Master of Science

The improvement in ionic conductivity of latex binder using Styrenesulfonic acid sodium salt hydrate (NaSS) for lithium secondary battery

The Graduate School of University of Ulsan

School of Chemical Engineering

Moongi Kim

The improvement in ionic conductivity of latex binder using Styrenesulfonic acid sodium salt hydrate (NaSS) for lithium secondary battery

Supervisor: Professor Eun-Suok Oh

A Dissertation

Submitted to
The Graduate School of the University of Ulsan
In partial Fulfillment of the Requirements
For the Degree of

Master

by

Moongi Kim

School of Chemical Engineering
University of Ulsan, Korea
February 2022

The improvement in ionic conductivity of latex binder using Styrenesulfonic acid sodium salt hydrate (NaSS) for lithium secondary battery

This certifies that the master's thesis

of Moon Gi KIM is approved.

Committee Chair Prof. Jun Bom Kim

Committee Member Dr. Tae Hee Kim

Committee Member Prof. Eun-Suok Oh

School of Chemical Engineering

University of Ulsan, Korea

February 2022

Abstract in Korean

리튬 이차전지의 구성은 크게 양극, 음극, 분리막 그리고 전해액으로 나뉜다. 특히 전도성 고분자(바인더) 소재는 전극의 활물질, 도전재, 집전체의 결착을 가능하게 하여 전극 내 전기적인 네크워크를 형성시키기 위한 필수 소재이다. 리튬 이차전지의 용량이 증가함에 따라 급속충전에 대한 수요 역시 늘고 있다. 하지만 짧은 시간 내 많은 에너지의 주입으로 전극에서는 부피 팽창에 의한 기계적 손상과 전기저항 증가로 인한 열적 손상이 발생한다. 따라서 급속충전 시 발생하는 전극 저항의 문제를 해결하기 위하여 바인더의 관점에서 이를 최소화하기 리튬 이온전도성을 향상시키고자 한다.

본 논문에서는 비공유 전자 쌍을 가지는 sulfonic group(SO_3H)이 포함된 monomer, NaSS(Styrenesulfonic acid sodium salt hydrate)를 도입하여 PS(Polystyrene)와 중합을 실시하였다. Styrene과 NaSS 함량 별 (PS-co-NaSS) core 구조를 만들고 아크릴계 monomer(AN, BA)와 개시제(GMA), acid(IA), hydroxy group 가지는 monomer(4-HBA)를 이용해 전극의 접착강도를 증가시키고 이온전도성 향상으로 전극 저항을 감소시켰다. 전도성 고분자(바인더)의 성능을 확인하기 위해 이온전도도 분석, 리튬 이온 transfer number, swelling test, 접촉각 측정, 전극 접착력을 측정하였다. 또한 NG(Nature Graphite)와 LFP(Lithium Iron Phosphate)에 바인더를 각각 적용시켜 전극을 만들고, coin-cell 형태로 half cell를 만들었다. 최종적으로 전기화학적 성능을 평가하기 위하여 수명, 율속, 임피던스, 순환 전압전류법을 분석을 하였으며, NaSS 함량에 따른 전지의 성능을 비교 분석하였다.

Abstract in English

A lithium secondary battery (LIB) is largely divided into a positive electrode, a negative electrode, a separator, and an electrolyte. In particular, the conductive polymeric binder is an essential material for forming an electrical network within the electrode by enabling binding of the active material, conductive material, and current collector of the electrode. As the capacity of LIBs increase, the demand for rapid charging is also increasing. However, due to the injection of a lot of energy within a short time, mechanical damage due to volume expansion and thermal damage due to an increase in electrical resistance occur in the electrode. Therefore, in order to solve the problem of electrode resistance that occurs during rapid charging, it is intended to improve lithium-ion conductivity by minimizing this from the viewpoint of the binder.

In this paper, a monomer containing a sulfonic group ($–SO_3H$) having a lone pair of electrons, Styrenesulfonic acid sodium salt hydrate (NaSS), was introduced and polymerized with Polystyrene (PS). Create a core structure for each NaSS content (PS-co-NaSS) and increase the adhesive strength of the electrode using an acrylic monomer (AN, BA), an initiator (GMA), acid (IA), and a monomer with a hydroxy group (4-HBA). Electrode resistance was reduced by improving ionic conductivity. To check the performance of the conductive polymer (binder), ion conductivity analysis, lithium ion transfer number, swelling test, contact angle measurement, and electrode adhesion were measured. In addition, a binder was applied to the cathode and anode respectively in NG (Nature Graphite) and LFP (Lithium Iron Phosphate) to make an electrode, and a half cell in the form of a coin-cell was made. Finally, in order to evaluate the electrochemical performance, lifetime, rate, impedance, and cyclic voltammetry were analyzed, and the performance of the battery according to the NaSS content was comparatively analyzed.

Table of Contents

List of Figures

List of tables

1 Introduction

1.1. Lithium ion battery (LIB)

Recently, as the problem of global warming has become serious, efforts are being made all over the world to reduce greenhouse gases. Domestic and foreign automakers are moving toward replacing the internal combustion engine with eco-friendly electric vehicles (EVs).

A lithium secondary battery is a battery that can be charged and discharged through an electrochemical oxidation-reduction reaction using lithium as a raw material [1], [2]. Lithium is the lightest alkali metal and has the smallest ion diameter. It is used in small electronic devices such as smartphones, tablet PCs, and notebook computers because of its high ion mobility and miniaturization of batteries (having high energy density). In addition, it does not contain environmental control substances such as Cd, Hg, and Pb, which are the materials of existing batteries, and it has the advantage of being recyclable and is eco-friendly.

Lithium-ion batteries are divided into four types: cathode, anode, electrolyte, and separator. Due to the oxidation-reduction reaction of the anode and cathode materials, electrons separated from lithium ions in the glycolysis process move to the anode and cathode along the wire, and in the case of charging, lithium ions move from the anode to the cathode. In the case of the positive electrode, it is an important material that determines the lifespan, capacity, and output of a battery. Representative active materials include $LiCoO_2$ (LCO), $LiFePO_4$ (LFP), $LiNiMnCoO_2$ (NCM), and $LiMn_2O_4$ (LMO). The anode serves to absorb and release lithium ions, and graphite is typically used. The separator plays a role in physically separating the anode and the cathode, should not be reactive with the electrolyte, and should have a pore structure that allows ions to pass through. PE

or PP is used as a typical separator material. The electrolyte requires low chemical reactivity and high ionic conductivity to transport ions, and $LIPF_6$ is a representative electrolyte [3], [4].

1.2. The characteristics of electrode materials

1.2.1. Anode active materials

Graphite, which has low electrochemical reactivity, structural stability, and low cost, is widely used as the anode materials. As shown Table 1, graphite is divided into natural graphite and artificial graphite [5], [6]. Nature graphite is lower than artificial graphite and exhibits high lithium ion storage capacity. However, due to the large surface area and the irregular structure, the edges are peeled of by permeation or decomposition reaction of the electrolyte, resulting in a large irreversible reaction. Artificial graphite has a more stable structure than natural graphite, changes in the structure due to repeated insertion and desorption of lithium ions are small. Therefore, it is mainly used in batteries that require a long lifetime, such as electric vehicles. (EV).

1.2.2. Cathode active materials

Cathode material was a determined the lifespan, capacity, and power of a battery, and accounts for over 30% of the manufacturing process cost [7]. Multiple cathode materials are currently used in commercial LIB. As shown Figure 1, cathode materials are largely classified into lithium cobalt oxide (LCO, $LiCoO_2$), lithium iron phosphate (LFP, $LiFePO_4$), lithium manganese oxide (LMO, $LiMn_2O_4$), ternary battery NCM and NCA. LCO is a material with a layered crystal structure and is a typical lithium-ion battery material due to its high energy output. LFP is composed of iron, which is cheaper than the scarcity element cobalt, but shows similar performance. LFP has a disadvantage in that the ion diffusion rate is slow during charging, it has an olivine structure, excellent stability, and a high lifespan. [8], [9], [10] In case of LMO, the

price is lower than LCO, but it has disadvantage of being thermochemically unstable. NCM and NCA due to high cost of cobalt and improved performance by blending compared with other active cathode materials [11].

Table 1. Physical properties of active material for anode

Graphite Type	**D50μm**	**BET-SSA (m^2/g)**	**Capacity (mAh/g)**
Artificial graphite	16	1.2	280~360
Nature graphite	18	3.8	360~372

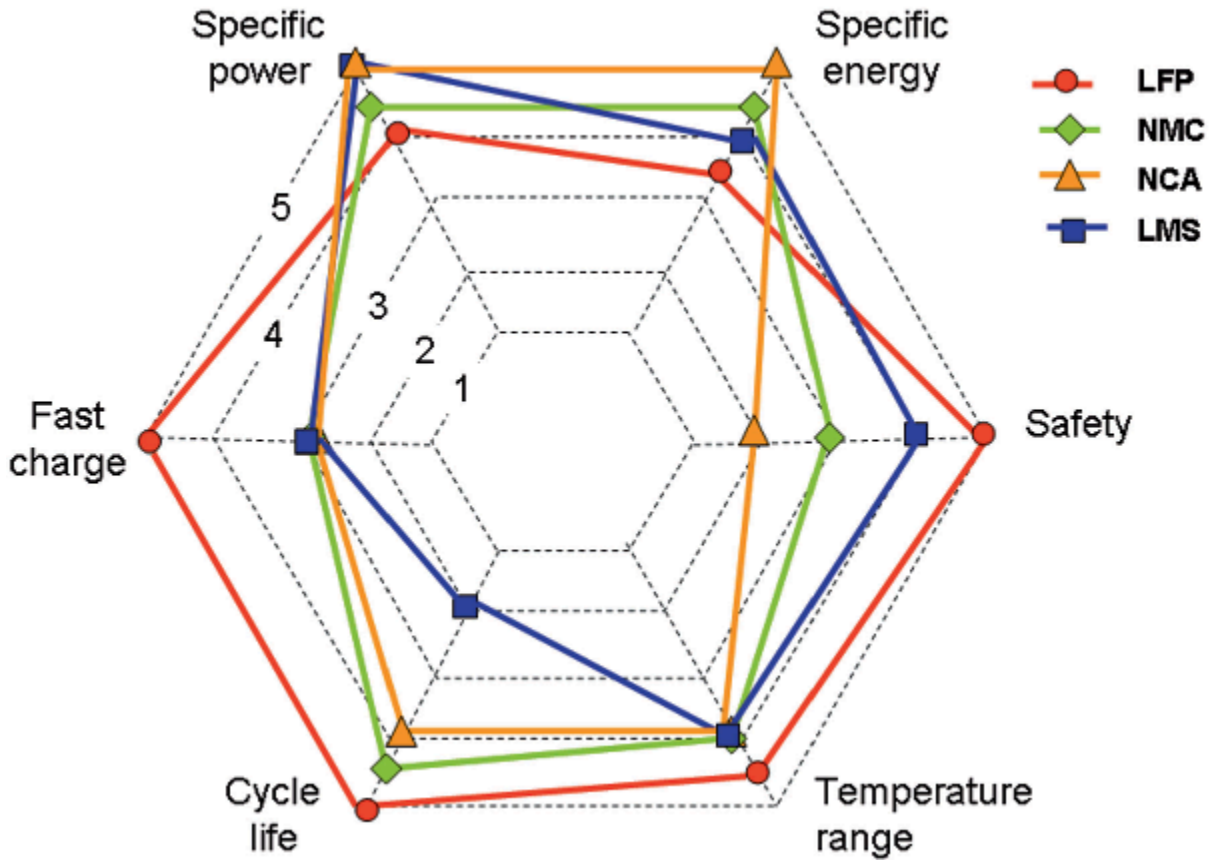

Figure 1. Rader diagram with performance characterization of cathode materials

2. Experimental Method

The main experimental methods used for this work are introduced in this chapter. These include the synthesis methods for graft copolymer, manufacturing of electrode slurry by solvent casting method, fabrication methods for half-coin cell, as well as chemical, physical and electrochemical characterization methods, and the setup used for a galvanostatic, an electrochemical dilatometer, a voltammetry, and an impedance experiment.

2.1. Materials

Styrene monomer(St, SAMCHUN), sytrenesulfonic acid sodium salt hydrate (NaSS, Alfa Aesar) were used as core monomer. Butyl acrylate (BA, SAMCHUN), acrylonitrile (AN, JUNSEI), hydroxybutyl acrylate (HBA, TGI) and itaconic acid (IA, SAMCHUN) were used as shell monomers. Sodium dodecyl sulfate (SDS, TGI) was used as surfactant, ammonium persulfate (APS, Sigma Aldrich) was used as initiator and Glycidyl methacrylate (GMA, SAMCHUN) was used as crosslinked agent.

2.2. Synthesis of new polymeric binder

The emulsion polymerization was carried out using a four-neck double jacket flask reactor with a stirrer, reflux condenser, feeding pump and nitrogen gas purging system during synthesis. The amount of NaSS monomers added to St monomer [12]. In the core step, first NaSS is added to styrene for each amount 2 and 7% emulsified. Second 30% pre-emulsion solution was added to the reactor and initiator solution stirred at 75℃. Third the remaining 70% of the solution was put in for 2 hours using a feeding pump. Finally, aging at 85℃ for 1 hour. Core-shell step, shell monomers were also polymerized in the same way as before core step. Additionally, an

initiator was added before aging step. Nitrogen purge was carried out at all of steps and the stirring speed was maintained at 170rpm.

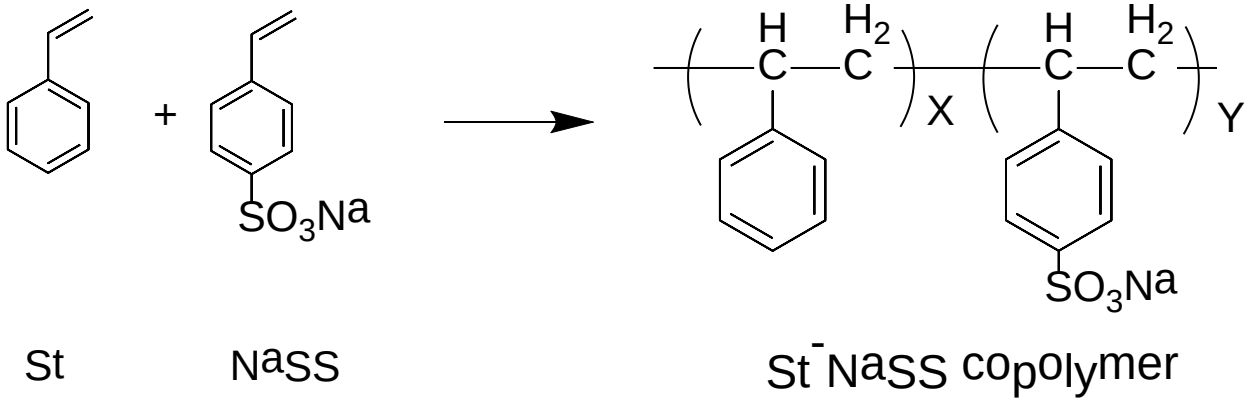

Figure 2. Chemical structure of Styrene-co- sytrenesulfonic acid sodium salt hydrate (St-NaSS)

2.3. Preparation of the slurry film for anode

The electrode composition was 92 wt.% nature graphite (918-II, d=16-21 μm, BTR. INC.), 2wt % carbon black (Super P), 1wt % CMC (Daicel FineChem Ltd., Japan), and 5wt % synthesized binder. The slurry was mixed by planetary centrifugal mixer (ARE-310, THINKY). First, nature graphite and Super P mixed under conditions of 1000rpm, 3min rotation and 3times. Then, the CMC was mixed tighter NG & Super P at 1200rpm, 3min rotation and 3times and the biner was mixed under conditions of 1500rpm, 1min. Deionized water was used as a solvent to control the slurry viscosity for all cases. The resultants were coated onto copper foil, dried in a convection oven at 65 °C for 30 min, and followed by vacuum drying at 65 °C overnight. The mass loading of electrodes was controlled to be around 3 ± 0.2 mg cm^{-2}.

2.4. Preparation of the slurry film for cathode

The electrode composition was 90 wt.% lithium iron phosphate (LFP, PULEAD TECHNOLOGY INDUSTRY CO., LTD.), 5wt % carbon black (Super P), 5wt % polyvinylidene fluoride (PVdF, Sigma Aldrich) binder used N-methyl-2-pyrrolidone (NMP, DAEJUNG) as solvent. The slurry was mixed by planetary centrifugal mixer (ARE-310, THINKY). First, LFP and Super P mixed under conditions of 1000rpm, 3min rotation and 3times. Then, PVdF was mixed tighter LFP & Super P at 1300rpm, 3min rotation and 4times. NMP solvent was used as a solvent to control the slurry viscosity for all cases. The resultants were coated onto aluminum foil, dried in a convection oven at 85 °C for 30 min, and followed by vacuum drying at 85 °C overnight. The mass loading of electrodes was controlled to be around 7.5 ± 0.3 mg cm^{-2}.

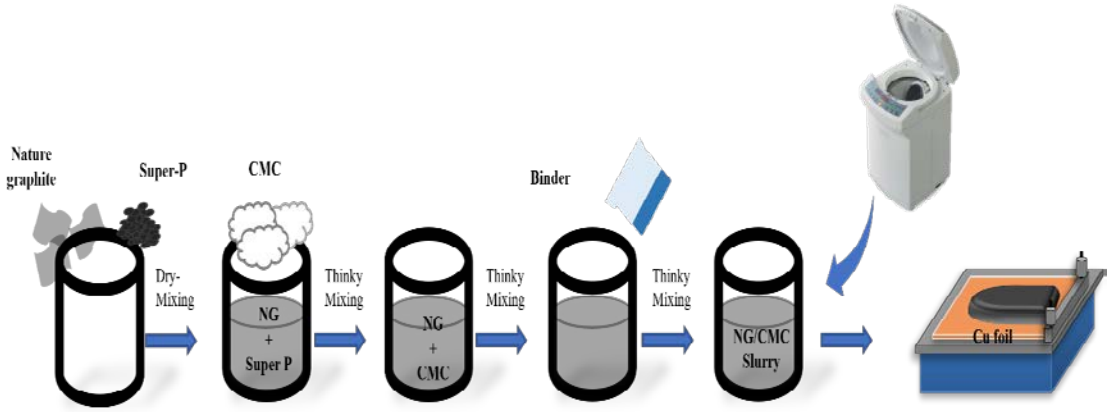

Figure 3. Schematic illustration of the manufacturing of electrode using of Styrene-co-sytrenesulfonic acid sodium salt hydrate (St-NaSS) as binder.

2.5. Fabrication of 2032 coin half cells

For electrochemical characterization, CR2032-type coin-half cells were assembled in an argon-filled glove-box using the graphite working electrode, Li chip as a counter and reference electrode, 1M $LiPF_6$ in ethylene carbonate (EC): ethyl methyl carbonate (EMC): dimethyl carbonate (DMC) 1:1:1 v/v% as an electrolyte, and polypropylene film (wellcos Ltd.) as separator. Each coin-half cells were rested one day before getting electrochemical tests.

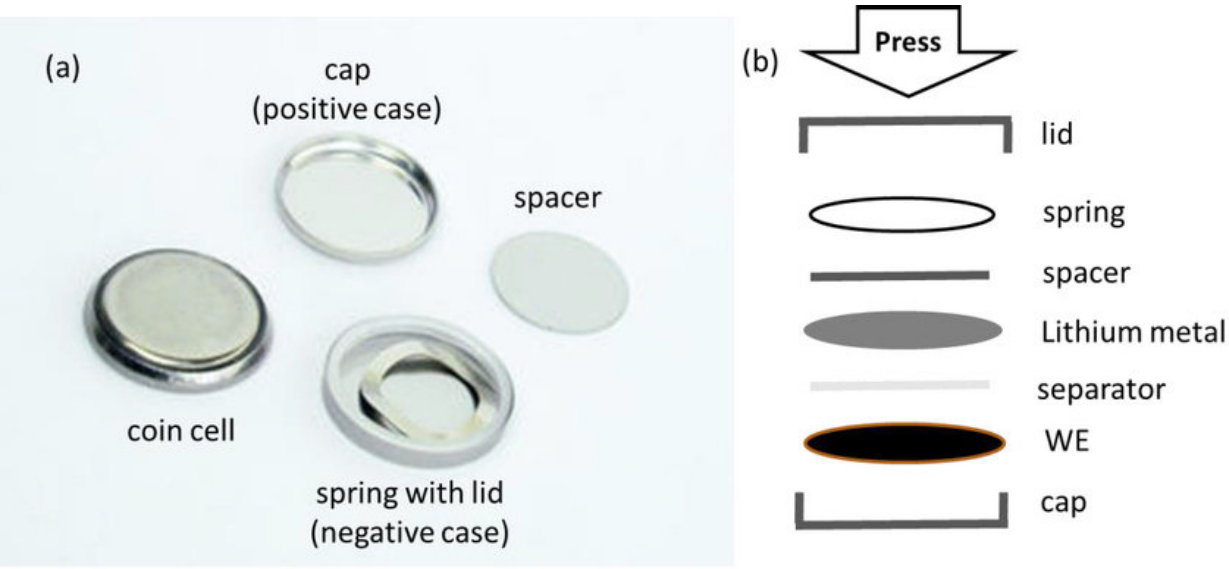

Figure 4. The components of 2032 coin-full cells.

2.6. Physical characterization

2.6.1. Zeta potential

Zeta potential (Zetasizer Nano ZS, Malvern Panalytical) is defined as the potential difference between the dispersion medium and the stationary layer of fluid attached to the particle. Zeta potential was performed using disposable folded capillar cells (DTS1070). This allows the measurement of the Zeta potential and the electric conductivity. The zeta potential value read the absolute value, and the larger the absolute value, the more stable.

2.6.2. Particle Size Analysis

The particle size and size distribution of the emulsion was measured using a (Zetasizer Nano ZS, Malvern Panalytical) apparatus based on a laser distribution light scattering technique. Several drops of the sample were dropped in to an aqueous medium (Deionized water) use the disposable sizing cuvette cells (DTS0012) and tri-layer system analyzes the signals to give the results of size and intendity distribution.

2.6.3. Infrared spectra of the synthetic polymeric binder

Fourier transform infrared spectroscopy (FT-IR), FT-IR spectra of polymer solution were obtained to confirm the existence of functional groups. FT-IR (Thermo Scientific Nicolet iS5 Infrared Spectrometer) was conducted in the range of 4000–400 cm^{-1} and it is capable to analysis of a liquid samples.

2.6.4. TEM of the synthetic polymeric binder

The morphology of the PS and PS-co-NaSS, particles was observed by Field Emission Transmission Electron Microscope (HT-7800, Hitachi). Diluted polymer solution was dropped on the 200 mesh copper grid and dry at room temperature. An image or diffraction pattern is obtained using electrons passing through a thin specimen, which is used for material correlation and structural analysis.

2.6.5. Electrolyte uptake

The electrolyte uptake of the binder films was also studied through an electrolyte absorption test. For preparing test samples, grafted copolymer was first dissolved in distilled water at room temperature and the binder and the thicker agent as CMC was mixed with 30:70 weight ratio. The binder films were prepared by a cast solution method in the Teflon evaporation dish at 60 °C overnight and each sample was weighted. Dried binder film was initially weighted (W_{before}), immersed in the electrolyte solution of (formula) at room temperature for various time range from 0.5 to 6 h, and weighed (W_{after}) again after the removal of excess electrolyte from their surface. The swelling ratio was calculated as:

$$\boldsymbol{S = \frac{W_{after} - W_{before}}{W_{before}} \times 100\%} \qquad \text{(Equation 2-1)}$$

2.6.6. Contact angle measurement

The contact angles of the polymer films are measured by an optical tensiometer (Theta life, Biolin Scientific) after 150 sec exposing to an electrolyte droplet. The binder films were prepared by a cast solution method in the Teflon evaporation dish at 60 °C overnight and each sample was weighted.

2.6.7. Adhesion strength

Using a texture analyzer (TA-PLUS, LLoyd Instruments Ltd.), the adhesion strength of graphite anode film was obtained by measuring the 180° peel strength of electrode strips with the peel rate of 100 mm min^{-1}. A wide of the electrode is casted by 40 mm and the thickness of anode film is arranged about 80-90 μm for before pressing and about 60-70 μm for after pressing and before the peeling test.

2.6.8. Electrode resistance

The electrical resistance of the thin films composed of electrode was measured using a 46 multipoint probe system (RM2610, HIOKI E.E. Co.). Prepare the electrode with 40mm width slitting and rolling press or not. Then measure the composite layer volume, surface and interfacial electrode resistance at regular intervals form the bottom to the top of the of the electrode.

2.6.9. Ionic conductivity of the synthetic polymeric binder

For preparing test samples, grafted copolymer was first dissolved in distilled water at room temperature and the binder and the thicker agent as CMC was mixed with 30:70 weight ratio. The binder films were prepared by a cast solution method in the Teflon evaporation dish at 60 °C overnight. All membranes had a thickness of about 349±10 μm. The polymeric membrane was sandwiching between two stainless steel electrodes in Swagelok cell with electrolyte. To examine the resistance to ion transport, the polymer film was sandwiched between two stainless steel (SS) electrodes in a 2032 coin-type cell. Before assembling the SS|polymer film|SS cell in an argon-filled glovebox, each polymer film was soaked in the carbonate electrolyte for 6 h. A BioLogic Science Instrument (VSP 350) was used for impedance spectroscopy analysis of the membranes. Complex impedance measurements were carried out in AC mode, in the frequency range 100 kHz-10 Hz, and 10 mV amplitude of the applied AC signal. The ionic conductivity calculated by following Equation (2):

$$\boldsymbol{\sigma = \frac{l}{AR_b}} \qquad \text{(Equation 2-2)}$$

Where, σ is a proton conductivity (S cm^{-1}); L is the thickness of the membrane; R is the resistance of the membrane (Ω) and A is surface area (cm^2).

2.6.10. Lithium-ion transition number of the synthetic polymeric binder

The Li+ transport number, (Li^+), through each polymer film was determined from EIS and potentiostatic polarization or chronopotentiometry methods using the electrolyte-swollen polymer film placed between two thin lithium chips in 2032 coin-cell. Herein, the frequency dependence of the cell impedance measured in a frequency range of 100 kHz – 10 Hz at different polarization level (OCV and 5-10 mV). After the impedance measurements, the cell was performed to the potentiostatic polarization

measurements with a applying constant potential (5-10 mV) for 2 hours. Then it continuously implead by impedance measurement at the applied potentials. The lithium transition number calculated by following Equation.

$$T_{Li^+} = \frac{I_s(\Delta V - I_0 R_0)}{I_0(\Delta V - I_s R_s)}$$

Equation 2-3

2.6.11. Morphology analysis as scanning electron microscopy

After Galvanostatic charge-discharge test, the cells were disassembled in an argon-filled glove box. The electrodes were washed with anhydrous dimethyl carbonate (DMC) to remove the electrolyte residues. The morphology of surface of the graphite electrode was operated by field-emission scanning electron microscopy (FE-SEM, Jeol, JSM-6500F).

2.7. Electrochemical properties

2.7.1. Galvanostatic charge-discharge test for anode

The electrochemical properties were conducted by the cycling performances in the voltage window of 0.005 to 1.5 V at 0.1 C for the first 2 cycles, and 0.5 C for the next 100 cycle using as the TOSCAT-3100 system (TOYO system. Co., LTD Japan). The rate capacity test was carried out at various current rate range of 0.1C to 10C with final returning back to 0.1C current rate and each current rate is scanned 10 times at related constant current rate.

2.7.2. Voltammetry and Impedance analysis

Cyclic voltammograms (CV) of the coin-half cell can be recorded at the different scan rates within a voltage range of 0.005 to 1.5 V as a BioLogic Science Instrument. The CV performed at various scan rates (such as 0.1, 0.2, 0.5, 1.0, 1.5, 2.0, 5.0, and 10 mV s^{-1}) were preformed to determination of the Li-ion insertion into the nature graphite anodes. Herein, the Randles-Sevcik equation[13–16] describes the effect of scan rate on peak currents to calculate the diffusion coefficient of lithium ion in an electrode:

$$\mathbf{I_p = 2.69 \times 10^5 A n^{3/2} C_0 D^{1/2} \nu^{1/2}} \qquad \text{(Equation 2-4)}$$

Here I_p, A, n, C_0, D, and ν are the peak current, the electrode surface area, the number of electrons transferred, the concentration of reactants, the diffusion coefficient, and the scan rate, respectively.

Electrochemical impedance spectroscopy (EIS) was tested into potentiostatic mode that is fixed with AC amplitude of 10 mV and a frequency range can be scanned at the frequency range from 100 kHz to 0.01 Hz. The open circuit voltage (OCV) in EIS measurements was controlled 0.2 V

vs. Li/Li^+. In order to achieve an equilibrium state, all cells for EIS were relaxed for 2 h before measurement. Nyquist plot was fitted by the equivalent circuit as shown in Figure 5 where the R_s and R_{ch} is reported solution resistance and, charge transfer resistance, and W is the Warburg impedance of solid phase diffusion, respectively. In furthermore, the low frequency Warburg region of the EIS enables to calculate the diffusion coefficients of lithium ions.

$$D = 0.5\left(\frac{RT}{AF^2\sigma_\omega C}\right)^2 \qquad \text{(Equation 2-5)}$$

where *A*, *F*, *C*, *R*, and T are surface area, Faraday constant, concentration of lithium ions in solid, gas constant, and temperature, respectively[17,18]. σ_ω is indicated the slope of real part of impedance versus $\omega^{-0.5}$ (angular frequency in the Warburg region).

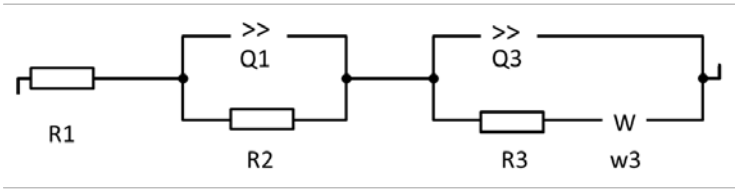

Figure 5. Equivalent circuit edition for impedance analysis.

3. Results and discussion

3.1. Physical characteristics of binder

3.1.1. B-TEM results

Figure 6, B-TEM image of polystyrene as a basis for polymerization of 0%, 2% and 7% NaSS at different contents to from St-co-NaSS structure. In the figure of (a), the core structure is formed in a round shape, and the particle decreases as the NaSS content increases. It can be confirmed that each particle is well attached to each other. A core having a St-co-NaSS structure and a monomer containing various acrylate, acid, and hydroxy groups were finally formed through emulsion polymerization to from a core-shell structure. (b) shows that 0%, 2% and 7% of all samples have different colors of core and shell parts.

3.1.2. FT-IR results

The FT-IR was measured by core with different NaSS content in polystyrene. As shown Figure 7 and Table 2, the wide band near 3284 cm^{-1} is assigned to water absorbed in the sample due to sulfonic acid groups are strongly hydrophilic [19], [20]. And the addition of sulfonate group to the polystyrene leads to a new absorption shows symmetric stretching vibration of SO_2. Then broad peak intensity at 1163 cm^{-1}, 1007 ~ 1100cm^{-1} corresponding to the functional sulfonic acid group -SO_3H. But it shows that 1167 cm^{-1} and 1063 cm^{-1} in the 0% sample, respectively, represent C=C bonds in the aromatic ring and OH bend. 0% sample is didn’t show peaks at 1080 to 1411 cm^{-1}, 1185 cm^{-1} and 936 cm^{-1}. [21], [22]

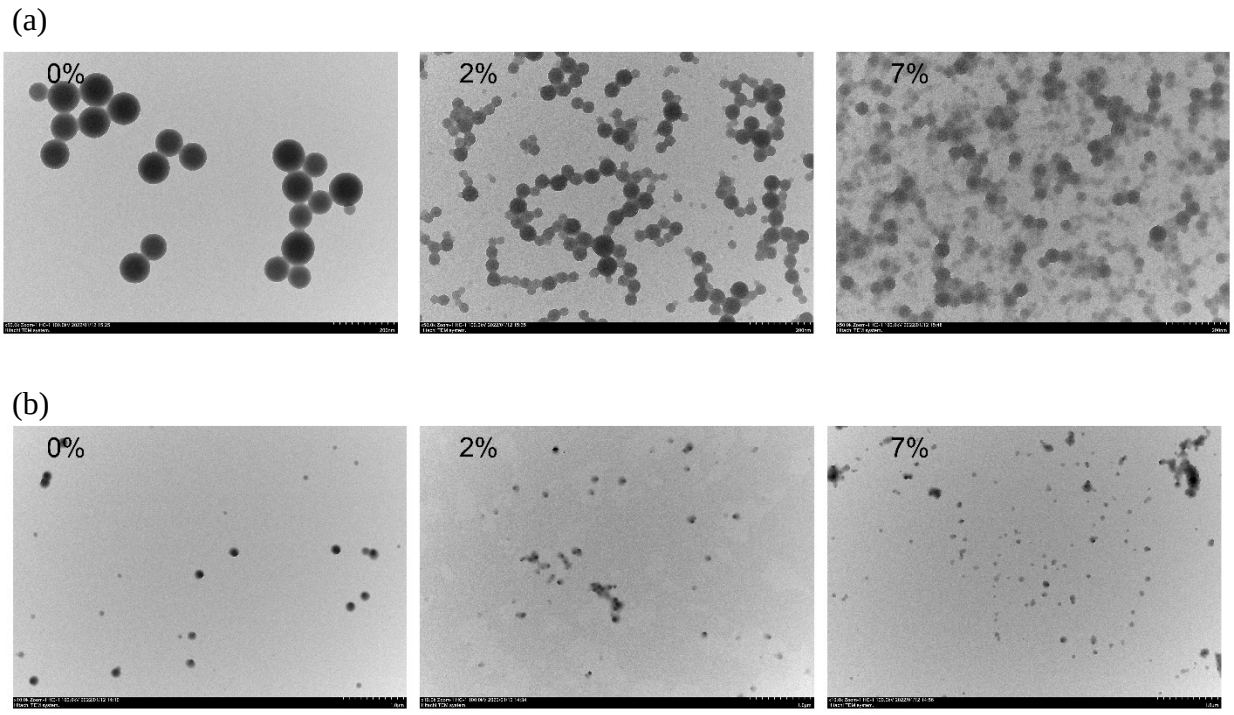

Figure 6. B-TEM image (a) core and (b) core-shell

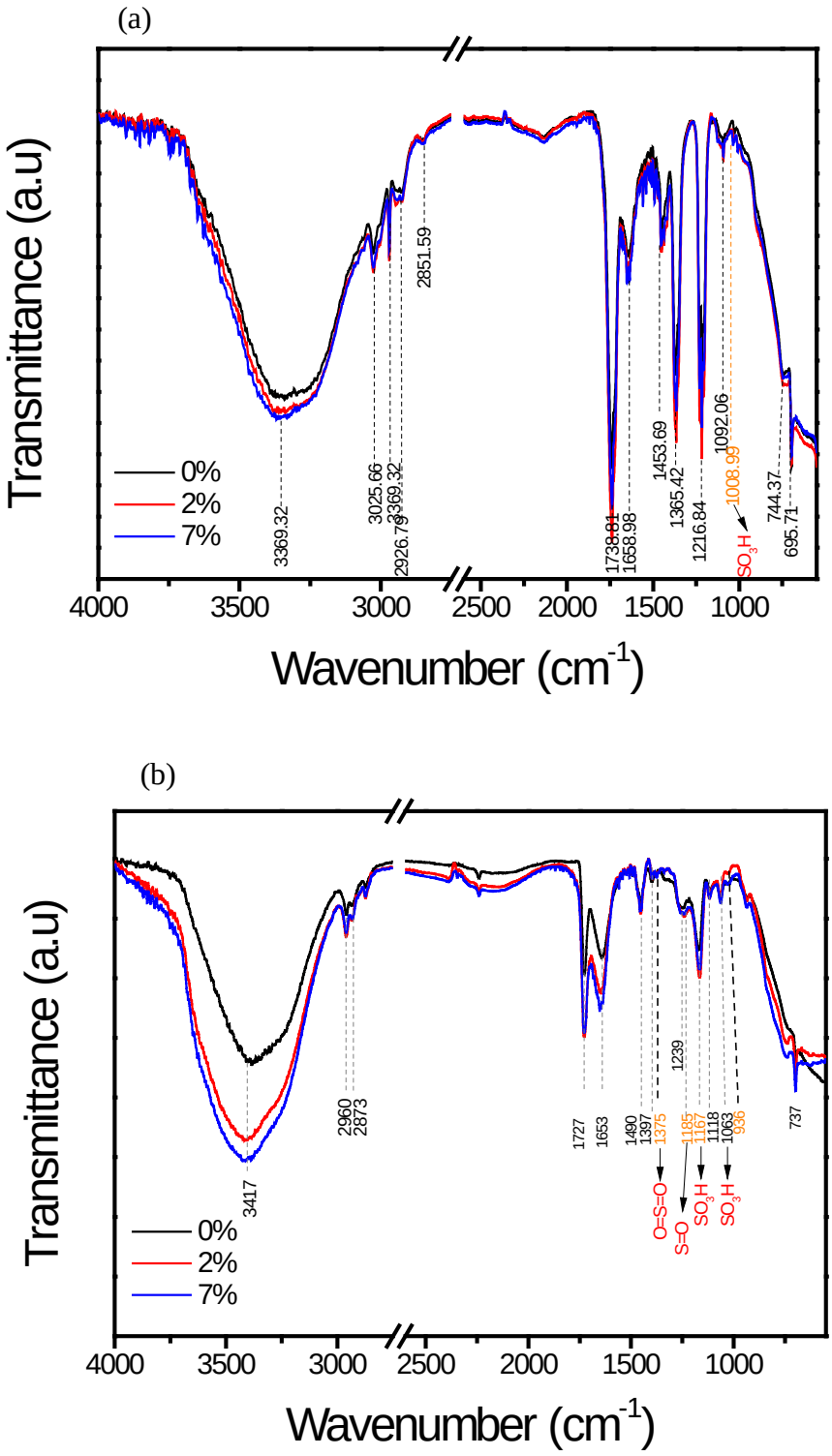

Figure 7. FT-IR spectrium of synthetic samples: core structure (a) and core-structure (b)

Table 2. FT-IR peak table of core shell structure

0%		**2%**	**7%**	
wavenumber	functional group	wavenumber	wavenumber	functional group
3417	O−H stretching	3417	3417	The wide band near 3284 cm-1 is assigned to water absorbed in the sample due to PSSA(sulfonic acid groups are strongly hydrophilic)
2960	asymmetric and symmetric CH_2 vibrations	2960	2960	
2873	polystyrene stretching bands	2873	2873	
1727	the C=O stretching vibration of carbonyl group	1728	1728	
1653	the stretching vibration of C=O group	1647	1653	
1559	C=C in-plane stretching of ring	1507	1559	
1541			1541	
1490		1491	1490	
1456		1452	1456	
1397	O-H bend	1397	1397	
		1375	1375	The addition of sulfonate group to the polystyrene leads to a new absorption of 1080-1411 cm-1. The absorption shows symmetric stretching vibration of O=S=O
			1339	
1239	o CH_2 and C–H wagging vibrations	1241	1240	
		1185	1187	S=O asymmetric stretching
1167	Vibration of C=C bonds in aromatic ring	1165	1166	broad peak intensity at 1163 cm–1 corresponding to the functional sulfonic acid group ($–SO_3H$)
1118		1118	1117	
1063	OH bend	1063	1063	broad peak intensity at 1007–1100 cm–1 corresponding to the functional sulfonic acid group ($–SO_3H$)
		936	936	(symmetric SO_2 stretch)
737	C−H out-of-plane bending	737	737	
697	phenyl out-of-plane bending	680	698	
			628	S–O stretching vibrations at 671 cm–1

3.1.3. Zeta potential results

Overall, the core zeta potential result is 40 to 60mv, indicating good stability. As shown Table 3 and 4, core shell, the sample without a sulfonic group was the lowest at -1.45mv, and the remaining 2%, 5%, 7% were nearby -30mv, showing stability.

3.1.4. Particle size analyze results electric conductivity

Table 3, 4 and Figure 8, below shows that, when NaSS is emulsion polymerized with styrene as a core, the particle size decreases as the sulfonic group increases. Conversely, electric conductivity tends to increase.

3.1.5. Ionic conductivity

After preparing the 10Ø binder film, ionic conductivity was calculated by the expression below.

$$\sigma = \frac{l}{AR_b} \rightarrow R = \rho\frac{l}{S} \rightarrow \rho = \frac{1}{\sigma} \quad \text{(Equation 3-1)}$$

l is the membrane thickness, A is the membrane area, R is the membrane resistance obtained from EIS experiments by an extrapolation of the real part of the impedance at high frequencies, As shown Figure 9 and table 5, the 7% containing the highest NaSS content showed the lowest membrane resistance. Therefore, the ionic conductivity increases as more sulfonic groups are contained.

3.1.6. Lithium-ion transport number

After preparing the 14Ø binder film, ionic conductivity was calculated by the expression below.

$$T_{Li^+} = \frac{I_s(\Delta V - I_0 R_0)}{I_0(\Delta V - I_s R_s)} \quad \text{(Equation 3-2)}$$

I_0, and I_s are initial and steady state current values, respectively, and R_0 and R_s are the initial and steady state measured resistances, respectively [23]. Figure 10 and Table 6, shows a plot of the current as a function of time ΔV=7mV, the Nyquist diagram applied ΔV=7mV are represented. From the Nyquist diagrams, R_0 and R_s were obtained for each membrane prepared. The result shows that, the value of Li^+ ion transport numbers increased as the NaSS content increases.

Table 3. core physical properties

	0%	**2%**	**7%**
Z-Average (d.nm)	100.3	75.09	55.20
Zeta-potential (mV)	-51.9mV	-49.6mV	-50mV
Conductivity (mS/cm)	4.24	5.13	7.91

Table 4. core-shell physical properties

	0%-HA	**2%-HA**	**7%-HA**
Z-Average (d.nm)	144.3	100.5	134.4
Zeta-potential (mV)	-1.45mV	-31.3mV	-29.7mV
Conductivity (mS/cm)	7.03	7.59	7.11

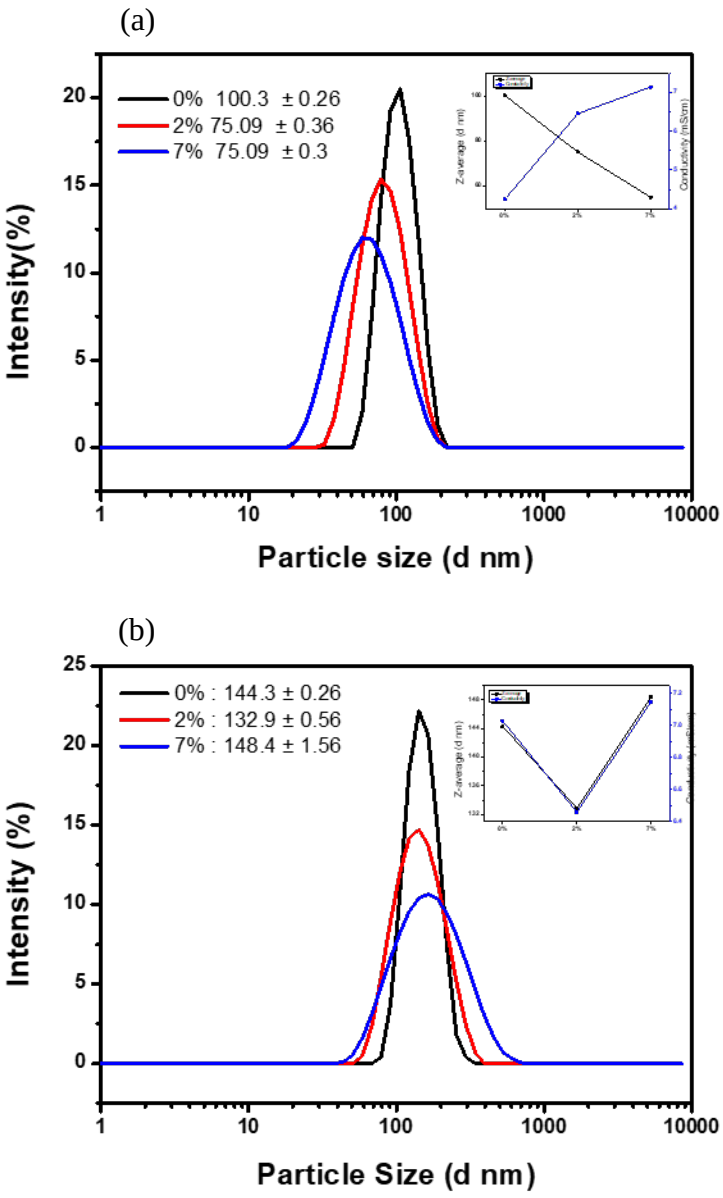

Figure 8. Particle size analysis of the St-NaSS (a) core, (b) core-shell binder samples

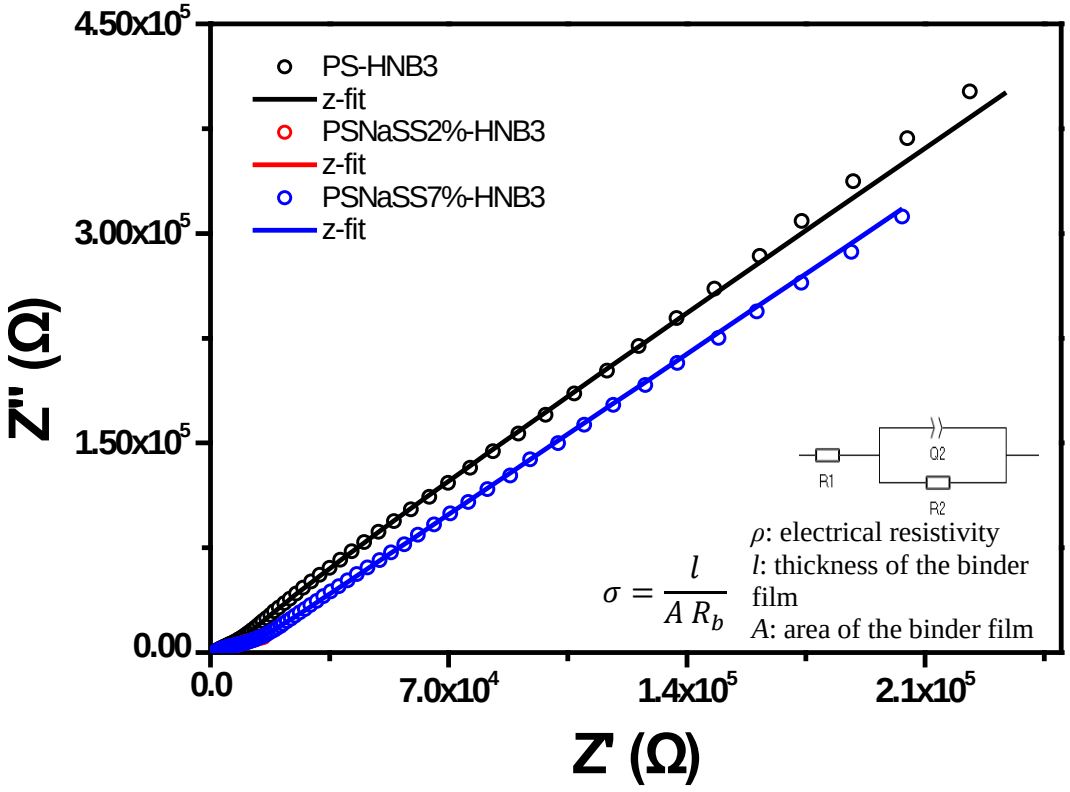

Figure 9. Ionic conductivity of the binder films

Table 5. Ionic conductivity

SS cell with electrolyte			
Sample	**0%**	**2%**	**7%**
Thickness (µm)	348.6	142.5	359.7
Area (cm^2)	0.79	0.79	0.79
Resistance (Ω)	53069	7299	8527
ionic conductive (Ω/cm)	8.32E-07	2.47E-06	5.34E-06

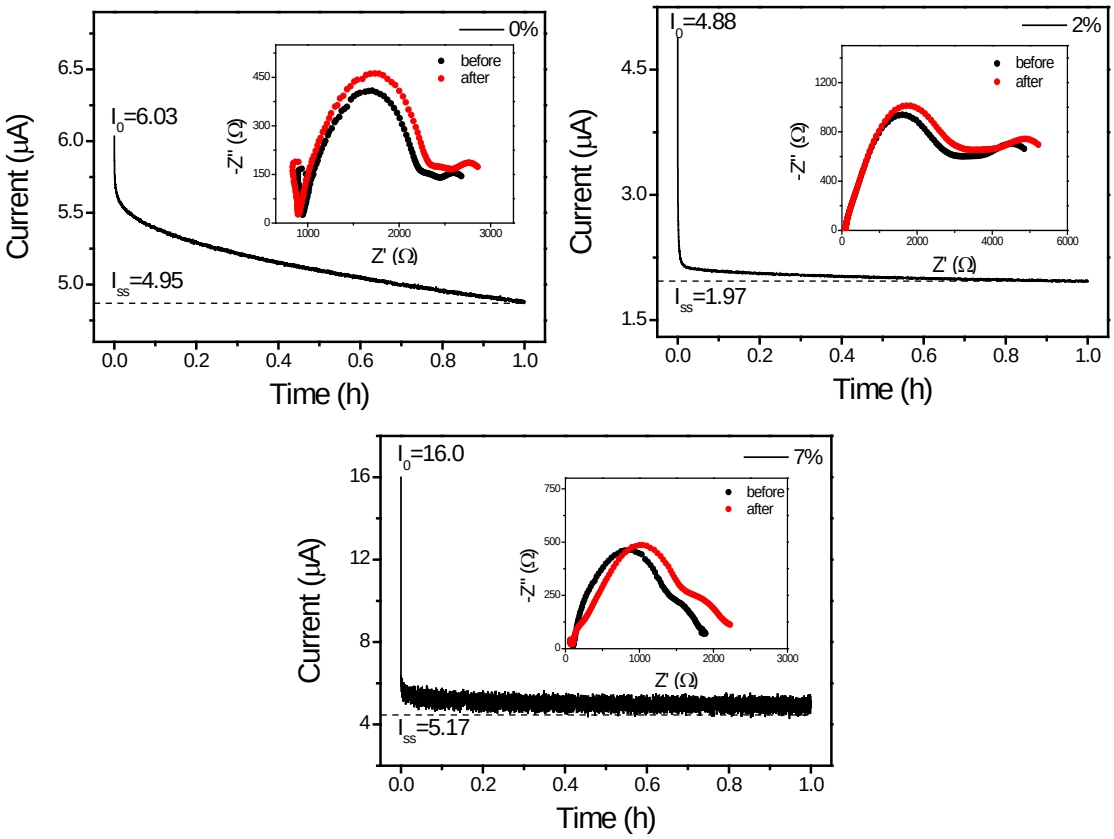

Figure 10. Lithium ion transport numbers

Sample	**0%**	**2%**	**7%**
$R_0\ (\Omega)$	2852.00	6184.00	1868.00
$I_0\ (\mu A)$	6.03	4.88	16.00
$R_S\ (\Omega)$	4492.00	6389.00	2499.30
$I_0\ (\mu A)$	4.95	1.97	5.17
$\Delta V\ (mV)$	7.00	7.00	7.00
t_{Li^+}	0.55	0.96	0.99

Table 6. Li^+ transition numbers of results

3.1.7. Dispersion stability results

Turbiscan stability index (TSI) is represents the degree of change in the dispersion and emulsion stability of the binder sample as a stability index, and the higher the TSI value, the lower the stability [24]. As shown in the Figure 11 below, 0%, 2% and 7% samples showed overall stability, and the TSI result increased for the first 2 hours, and then showed a stable result. Overall, all samples are stable.

3.1.8. Electrolyte uptake results

The electrolyte uptake results are an experiment showing how much the electrolyte permeates itself into the binder film [25]. Biner film was continuously soaked in electrolyte for up to 6 hours, and weights were measured for 30 minutes, 1 hours, 3 hours, and 6 hours. Showing at the Figure 12, below after 3 hours, containing 7% of NaSS monomer uptakes the electrolyte the most.

3.1.9. Contact angle results

Basically, the contact angle is the angle between gas or liquid drop and solid surface when droplet has a thermodynamic equilibrium with a solid surface. High contact angle means low wettability and hydrophobic property, on the other hand, low contact angle corresponds to high wettability and hydrophilic property [26], [27]. As shown Figure 13 and Table 7, when the initial contact angle and contact angle after 150 seconds were compared, the sample without NaSS showed the lowest difference in contact angle, and the 7% amount with NaSS content showed the largest difference.

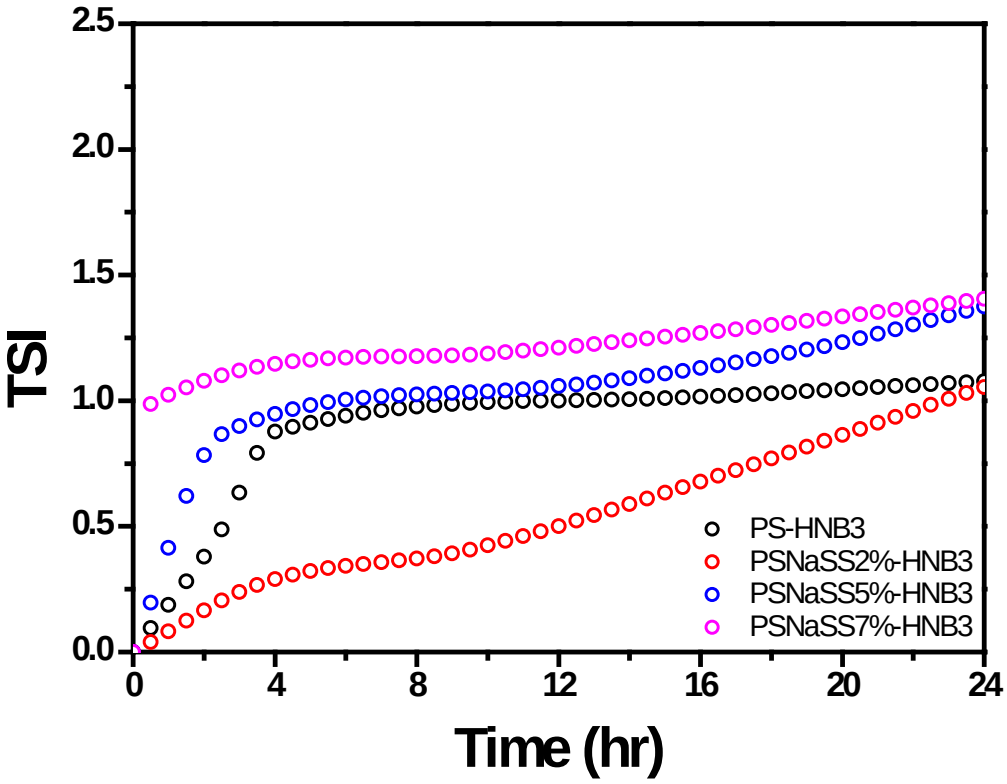

Figure 11. Dispersion stability results

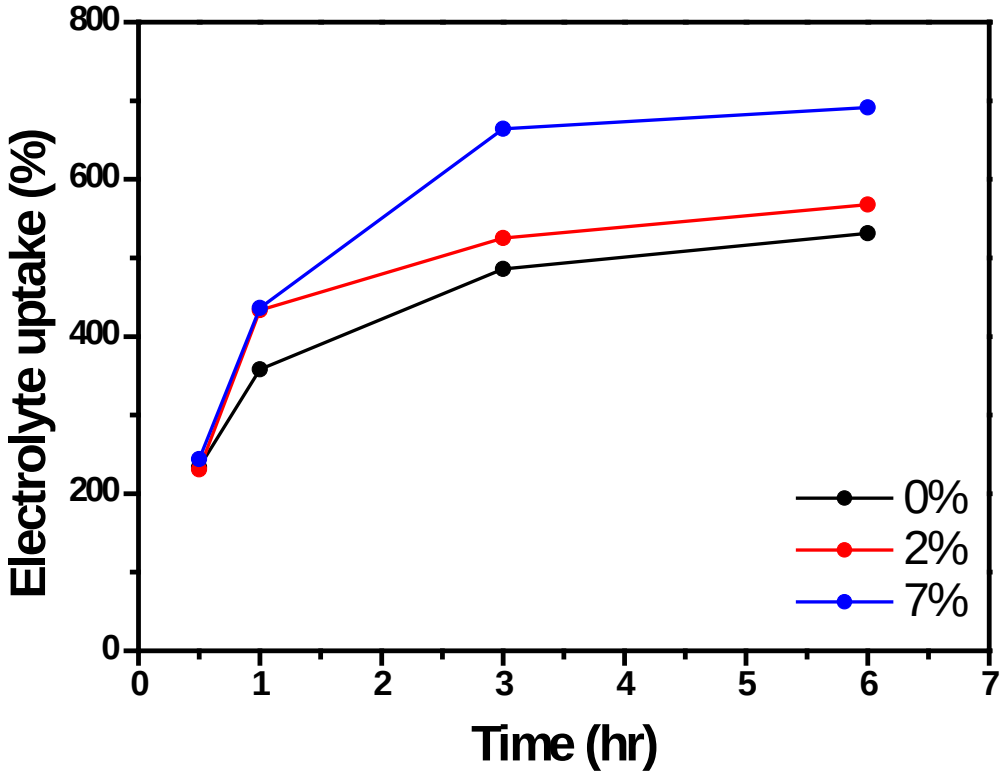

Figure 12. Amount of electrolyte uptake of polymer films immersed in electrolyte solutions

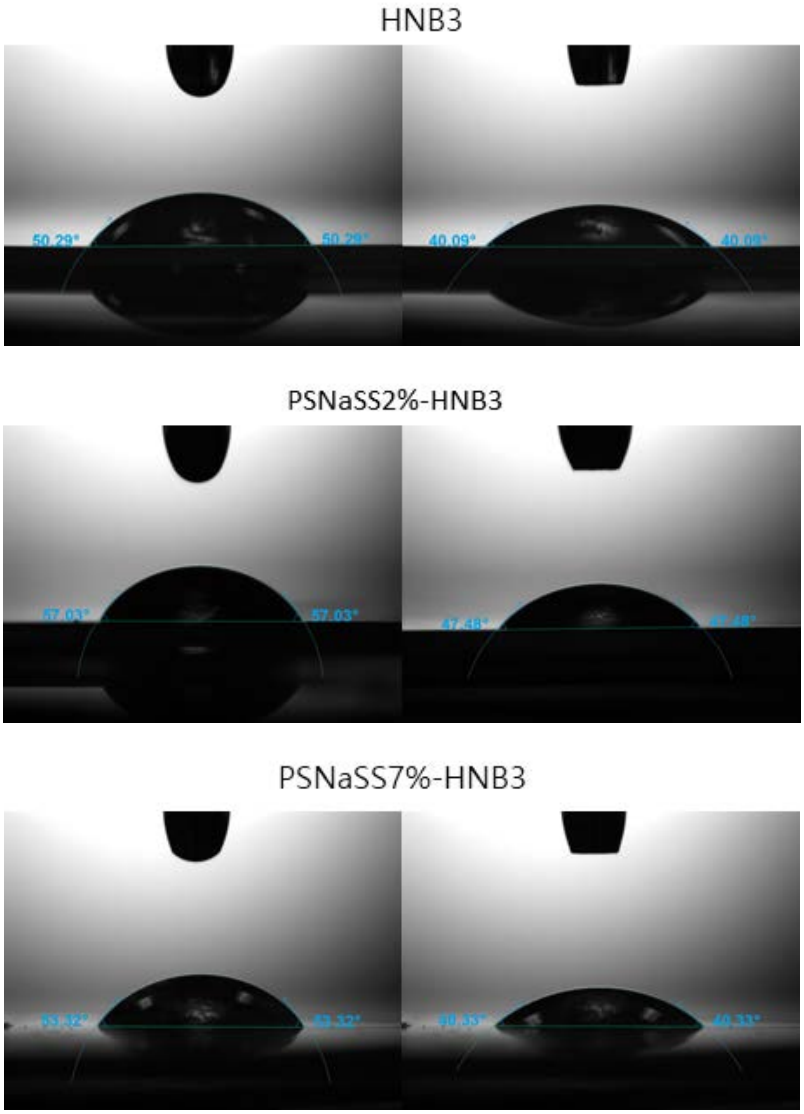

Figure 13. Photographs of the moment that electrolyte was dropped at binder films at binder films at 0s and 150s

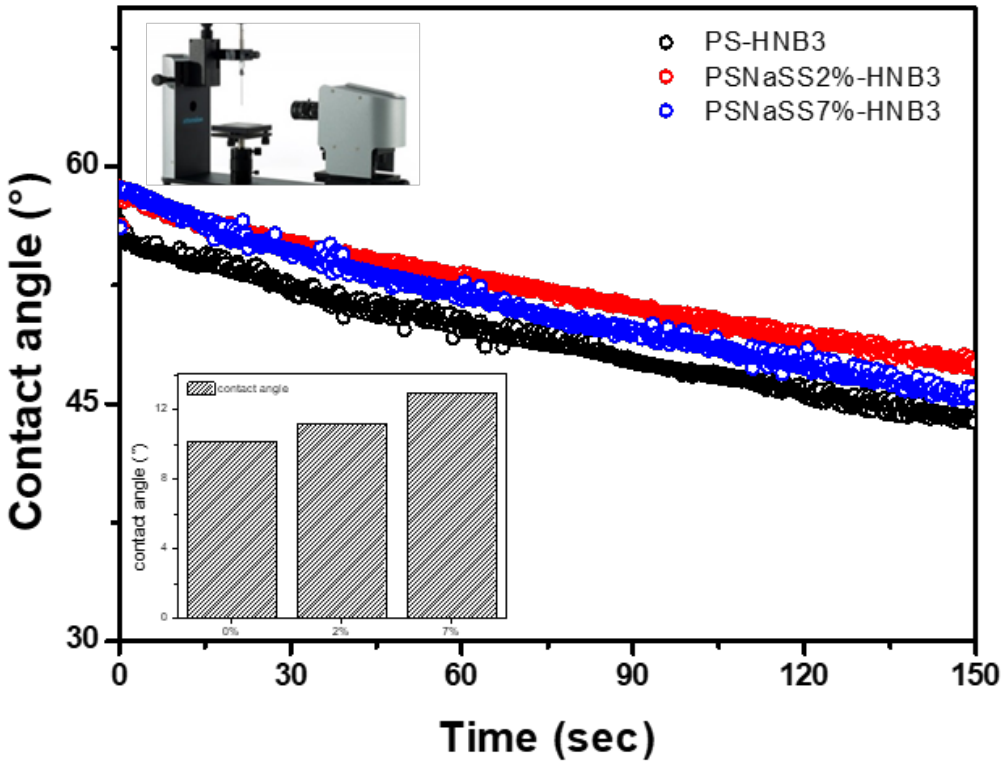

Figure 14. Amount of electrolyte uptake of polymer films immersed in electrolyte solutions

Table 7. Contact angle comparison

	Time (0s)	**Time (150s)**	**Contact angle comparison**
0%-HA	50.29˚	40.09˚	10.2˚
2%-HA	54.64˚	42.61˚	11.2˚
7%-HA	53.32˚	40.33˚	13.0˚

3.2. Nature graphite for anode

3.2.1. Electrode resistivity & resistance and adhesive strength of anode results

As shown Figure 15, the electrode was used to measure the volume, interface, and surface resistance of the composite layer. According to the figure, 2% and 7% content of NaSS showed less resistance than 0%. This was influenced by the sulfonic group. In the adhesion test of graphite electrode film, the bonding strength between the current collector and the slurry can be expected. As a result of the interface resistance, containing 7% NaSS showed the higher than 0%.

3.2.2. Cycle and rate capability results

In this experiment, specific capacity (mAh/g) of the electrodes containing each different binder ratio of styrene and NaSS is shown in Figure 16. When the electrode has large NaSS amount, the electrode has the highest specific capacity and show stable performance in cyclic test. During 100cycles, the specific capacity NaSS7% sample showed the highest and most stable results than 0%, 2% samples. In the result of rate capability test is displayed in Figure. At a low scanning rate up to 1C, the specific capacity of 7% was higher than that of 0%, 2% samples except for 0.1C. At high scanning rate form 2C to 10C, 2% showed the lowest capacity, and 7% still showed the highest capacity. When the 0.1C rate was returned, 2% display a lower does than 7%

3.2.3. EIS and Cyclic voltammetry (CV) results for anode

The EIS of the graphite electrode was measured at OCV and discharging/charging, 0.2V after two pre-cycle at 0.1C followed by two more cycles at 0.5C. EIS results are displayed in this Figure 17 (a). Semicircle was drawn the least in the 7% containing the most NaSS than in the 0% not containing it. In addition, the size of semicircle decreased as the amount of NaSS increases, which indicates that the size of the resistance decreased. Due to the of NaSS effect, as shown graph and table, it can be expected that R_{ct} is a value that is 7% easier for lithium-ion migration than 0% NaSS content. Diffusion coefficient results were also same situation. CV was measured form 0V to 3.0V to apply as nature graphite electrode. As shown Figure 17 (b), current peak was larger in the 2% and 7% samples containing NaSS than 0%.

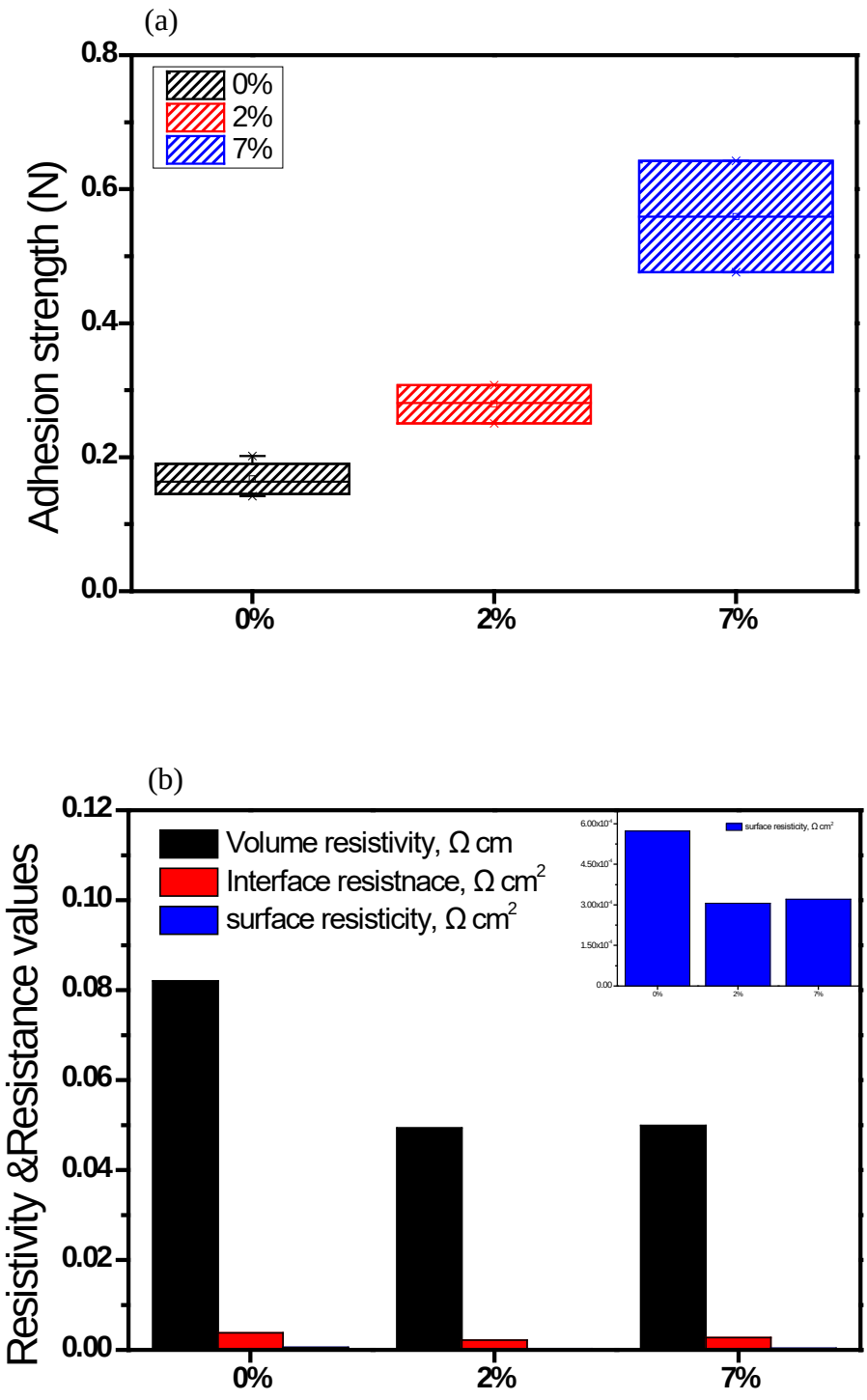

Figure 15. Adhesion strength of nature graphite electrodes (a) and resistivity and resistance of anode sheet (b)

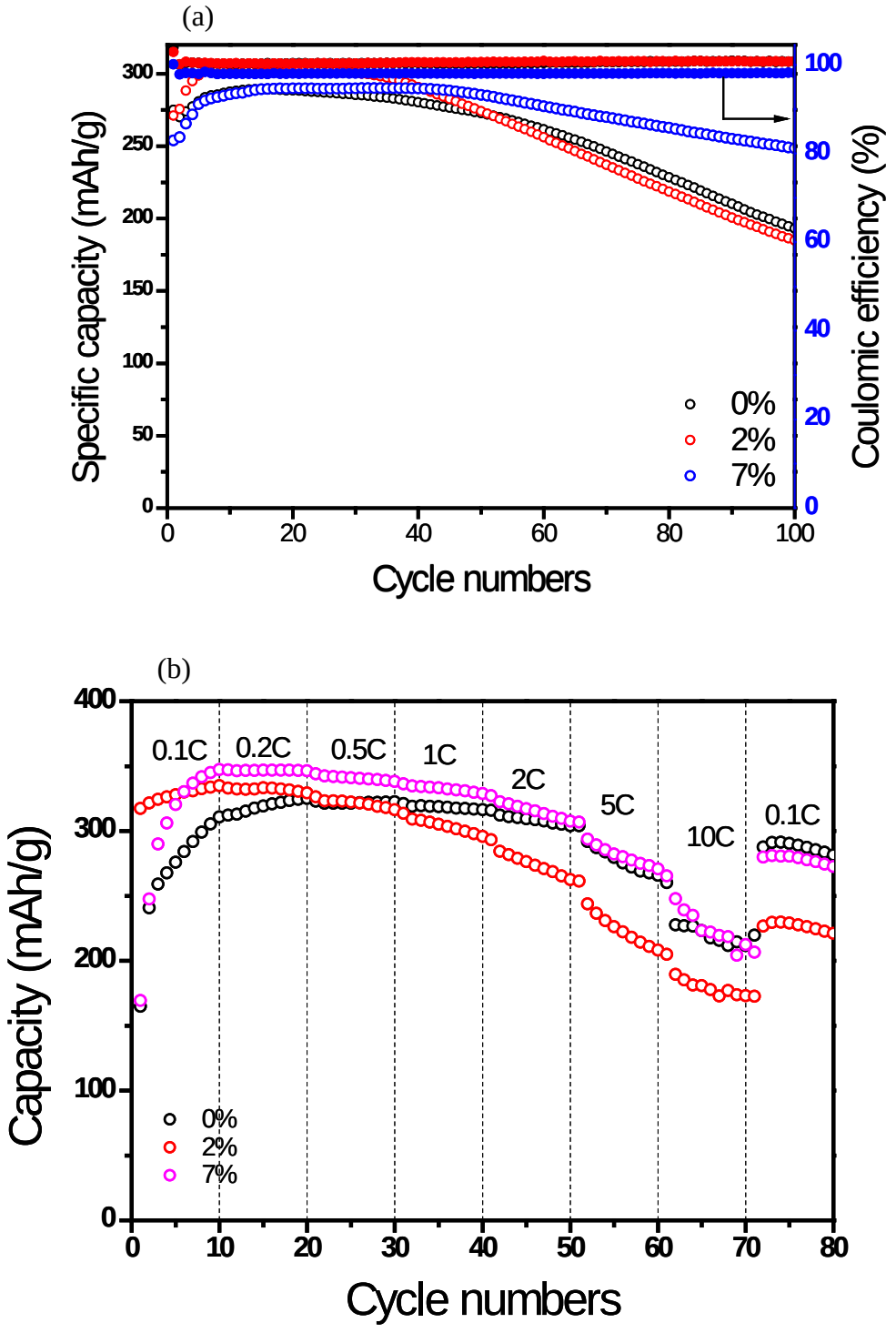

Figure 16. (a) Cyclic performance and Coulombic efficiency and (b) rate capability of the electrodes using each binder, current changes for every 0 cycles

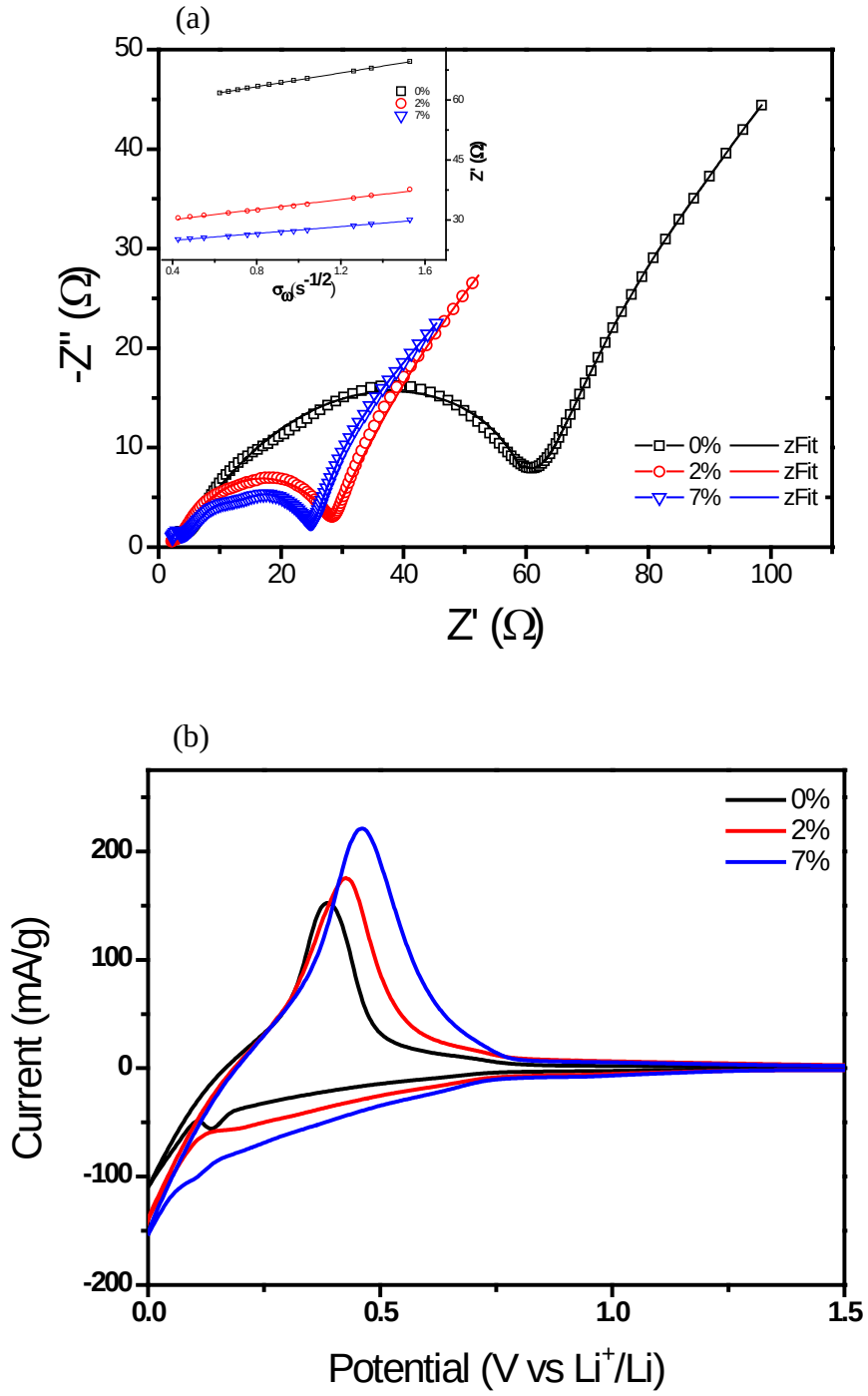

Figure 17. (a) EIS data expressed as Nyquist plot of flesh anode with various binders (b) and Cyclic voltammograms as scan rate 0.2 mV/s

Table 8. EIS results of graphite electrodes

Sample	R_s (Ω)	R_{SEI} (Ω)	R_{ct} (Ω)	R_{total} (Ω)	$\sigma\omega$(Ω/$S^{0.5}$)	$D_{Li+} \times 10^{-10}$(cm^2/S)
0%	2.85	13.01	40.73	56.59	8.60	1.99
2%	1.53	3.56	26.30	31.39	6.33	3.68
7%	1.25	2.02	22.86	26.13	4.33	7.85

3.2.4. Thickness change after cycle test for anode

Measure the thickness of the electrode composite layer by fresh electrode and disassembling the coin-cell that has completed 100 cycles charge and discharge test. As shown Figure 18, the thickness change was largest in 0% without a sulfonic group, and the thickness change gradually decreased as the content of the sulfonic group increased. It prevents the volume expansion of the composite layer in graphite under the influence of sulfonic groups during lithium ion insertion and desorption.

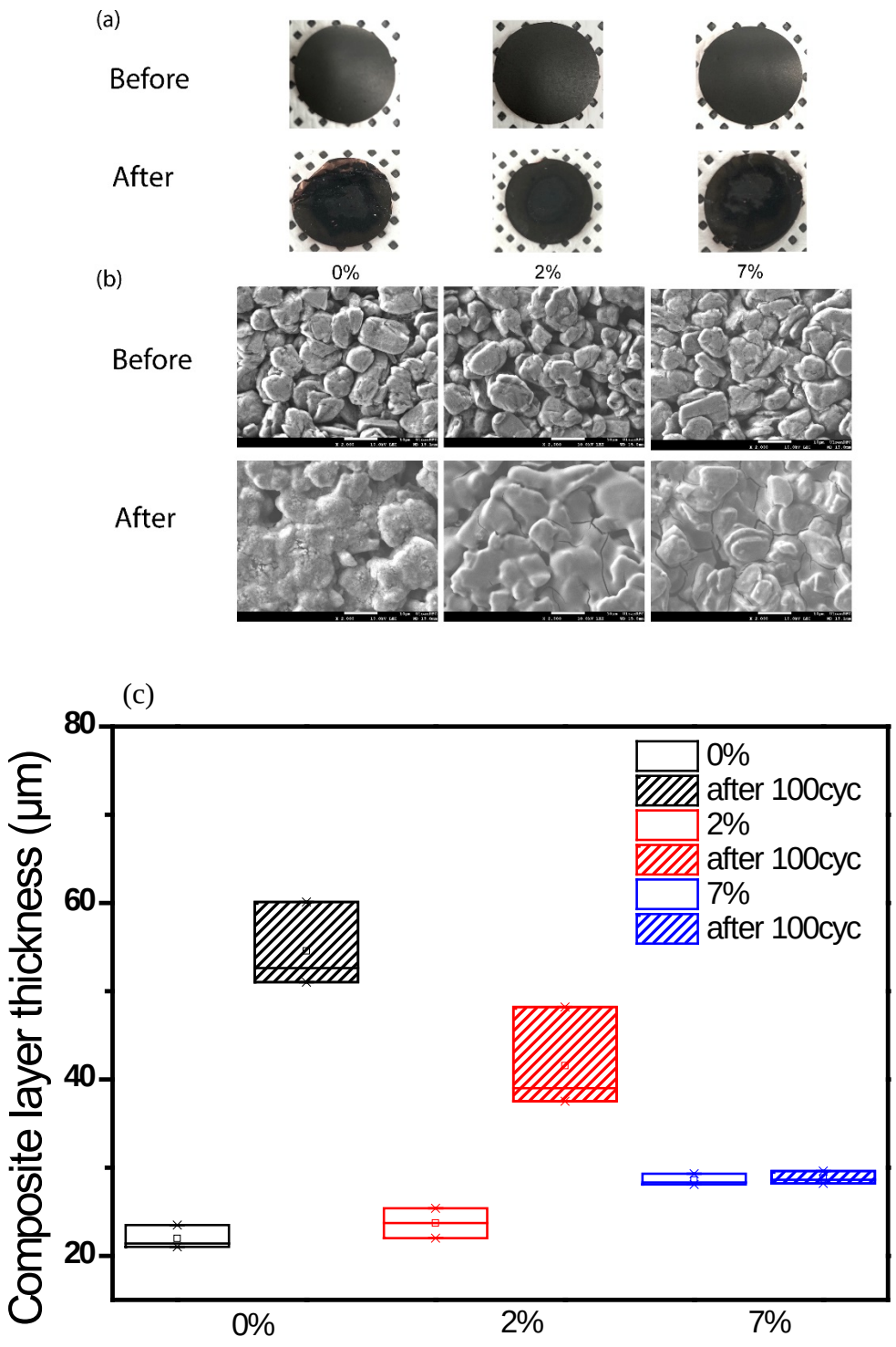

Figure 18. (a) Graphite electrode with different binders before and after 100cycles: (a) photo-image of the electrode, (b) Top FE-SEM image with ×2000 magnifications and (c) difference of composite layer thickness

3.3. Lithium iron phosphate (LFP) for cathode

3.3.1. Electrode adhesive strength for cathode

In the adhesion test of LFP electrode film, the bonding strength between the current collector and the slurry can be expected. As shown Figure 19, containing 7% NaSS showed the highest value, and second sample was measured to be the highest at 2%. In conclusion, the adhesion is superior to PVdF. The commercialized PVdF binder was not affected by hydrogen bonding by the hydroxyl groups, so it was measured to have lower adhesion than the sample containing NaSS. Expect for PVdF, the results are same as in case of anode.

3.3.2. Electrode resistivity & resistance and adhesive strength of cathode results

The LFP electrode was used to measure the volume, interface, and surface resistance of the composite layer. According to the Figure 19 (b), expect for PVdF, the results are the same as in case of anode. 2% and 7% content of NaSS showed less resistance than 0%. This was influenced by the sulfonic group. In the adhesion test of graphite electrode film, the bonding strength between the current collector and the slurry can be expected. As a result of the interface resistance, containing 7% NaSS showed the higher than 0%.

3.3.3. Cycle and rate capability results

In this experiment, the specific capacity (mAh/g) of the electrodes containing each different binder ratio of styrene/ NaSS and comparative experiments with commercially available PVdF binders are shown in Figure 20. As a result of the experiment, it was as stable and efficient as when 7% was applied to the anode electrode, but in the case of PVdF binder, the efficiency rapidly decreased under 20 cycles. In the result of rate capability test is displayed in Figure. At a low scanning rate up to 1C, the specific capacity of 7% was higher than that of 0%, 2% and PVdF samples. And after different scan rates for 2 cycles each, performance was evaluated for 2 cycles at 0.2C, and then 100 cycles at 1C. As a result of the experiment, 7% still showed superior performance compared to PVdF.

3.3.4. EIS results for cathode

The EIS of the LFP electrode was measured at OCV and discharging/charging, 0.2V after two pre-cycle at 0.2 C followed by two more cycles at 1C. EIS results are displayed in this Figure 21. Semicircle was drawn the least in PVdF binder. The reason is that in the graph of the cycle test results, capacity value was under 10 mAh/g in less than 10 cycles, so it can be predicted that electrochemical reaction did not occur. For the remaining samples, resistance occurred inside the coin-cell because the electrode surface not clearly saw in the below Figure 21.

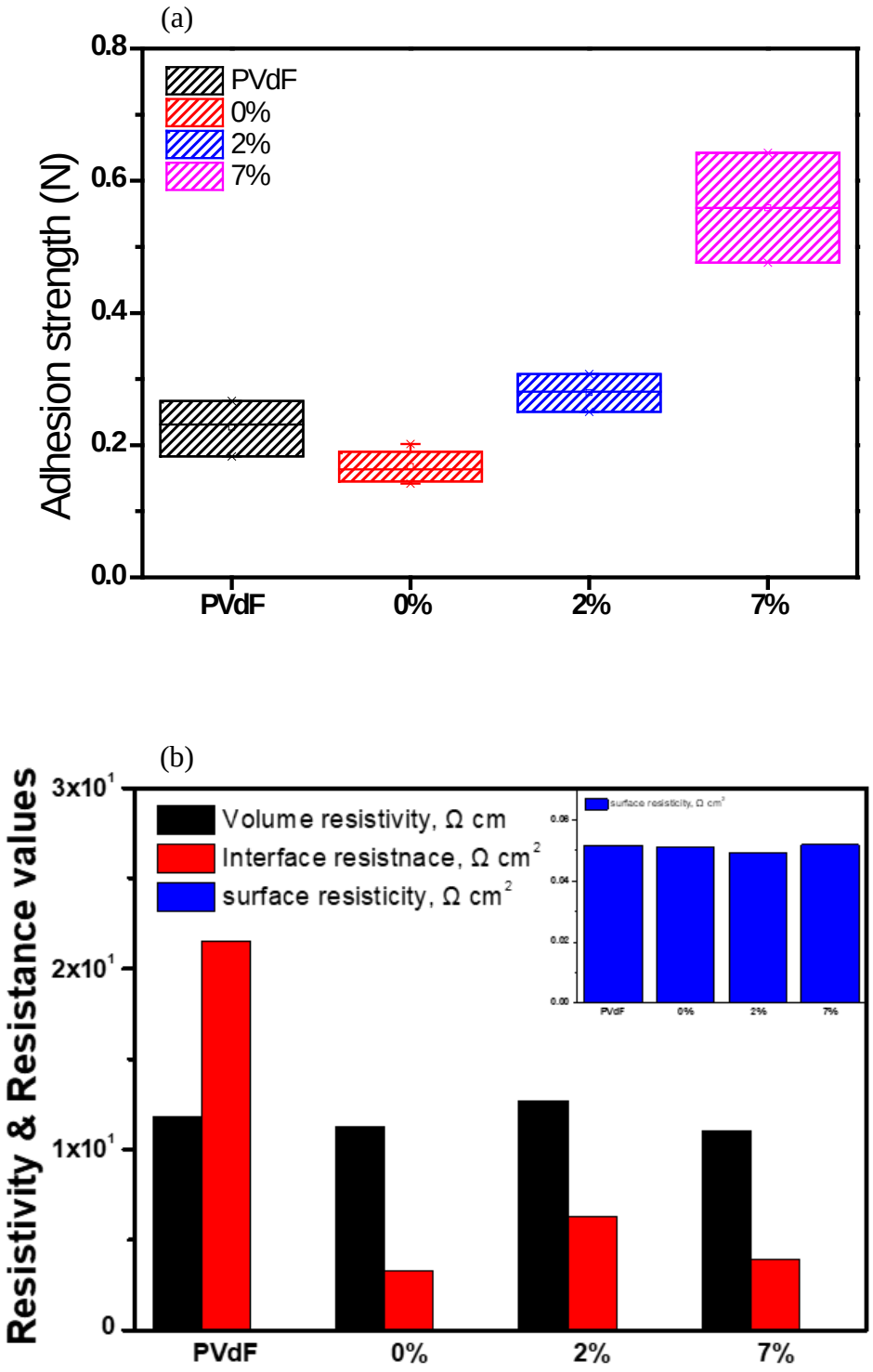

Figure 19. (a) Adhesion strength of the LFP electrodes containing different binders measured by 180° peel test (b) Sheet resistance of 65 μm thick LFP slurry films

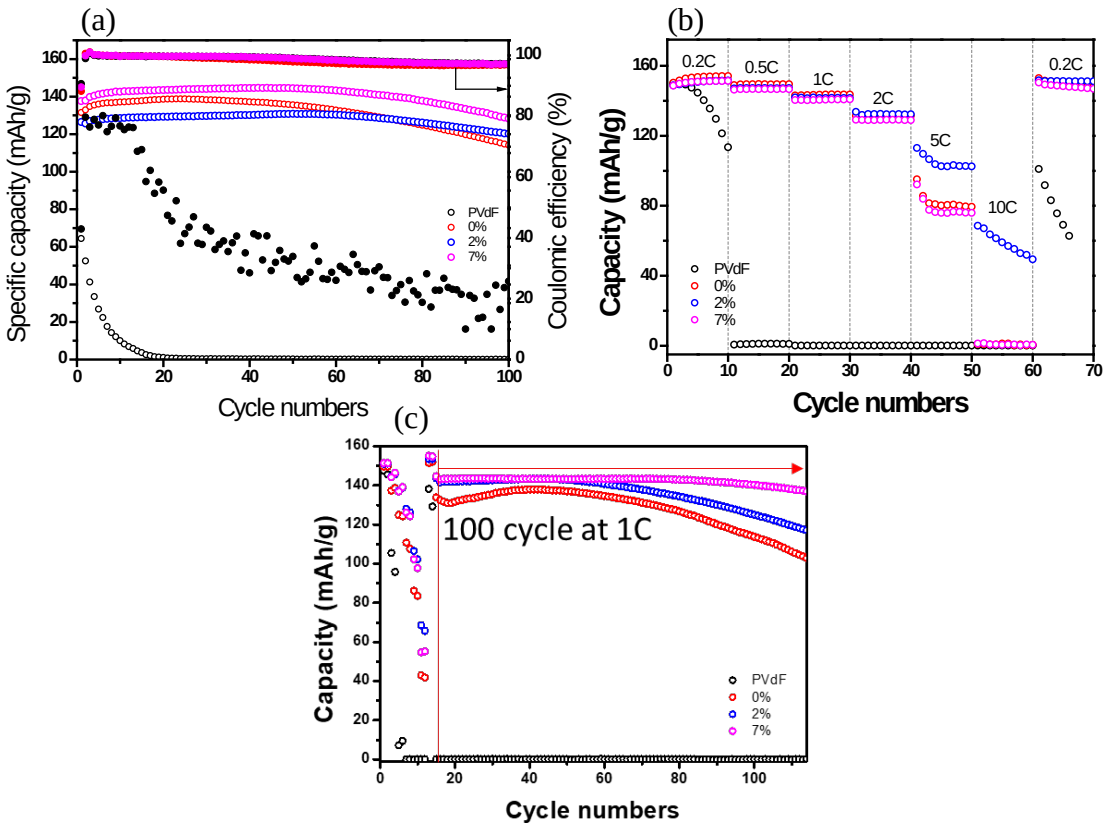

Figure 20. (a) Cyclic performance and Coulombic efficiency and (b) Rate capability of the LFP electrodes using each binder, current changes for every 10 cycles and (c) Rate capability of the electrodes using each binder, every 2cycles after after than go back to low current rate at 100cycles

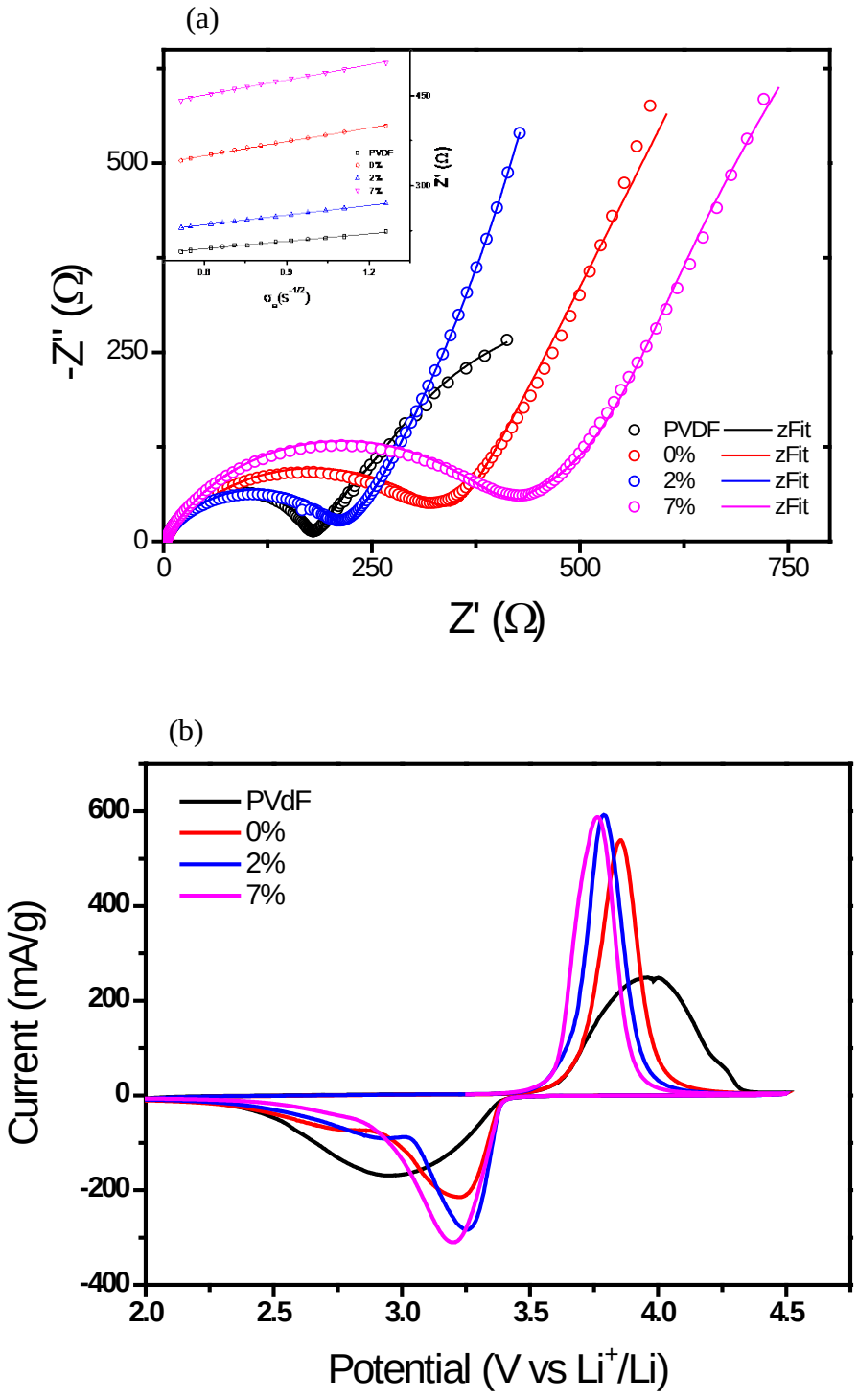

Figure 21. (a) EIS curve of LFP electrode with differen binders after precycling at 0.2C and two cycling at 1.0 C and (b) Cyclic voltammograms as scan rate 0.2 mV/s

3.3.5. Thickness change after cycle test and Cyclic voltammetry (CV) for cathode

As shown Figure 22 (a), measure the thickness of the electrode composite layer by fresh electrode and disassembling the coin-cell that has completed 100 cycles charge and discharge test. In case of PVdF binder, the electrochemical reaction did not occur, because the cell capacity was close to 0 mAh/g in the initial cycle. Therefore, there was almost no change in the thickness of the composite layer before and after the cycle test. Remaining samples, difference in thickness change gradually decreased as the content of the sulfonic group increased, as in the anode. CV was measured form 2.0V to 4.5V to apply as LFP electrode. As shown Figure 22 (b), was larger in the 2% and 7% samples containing NaSS than PVdF and 0%.

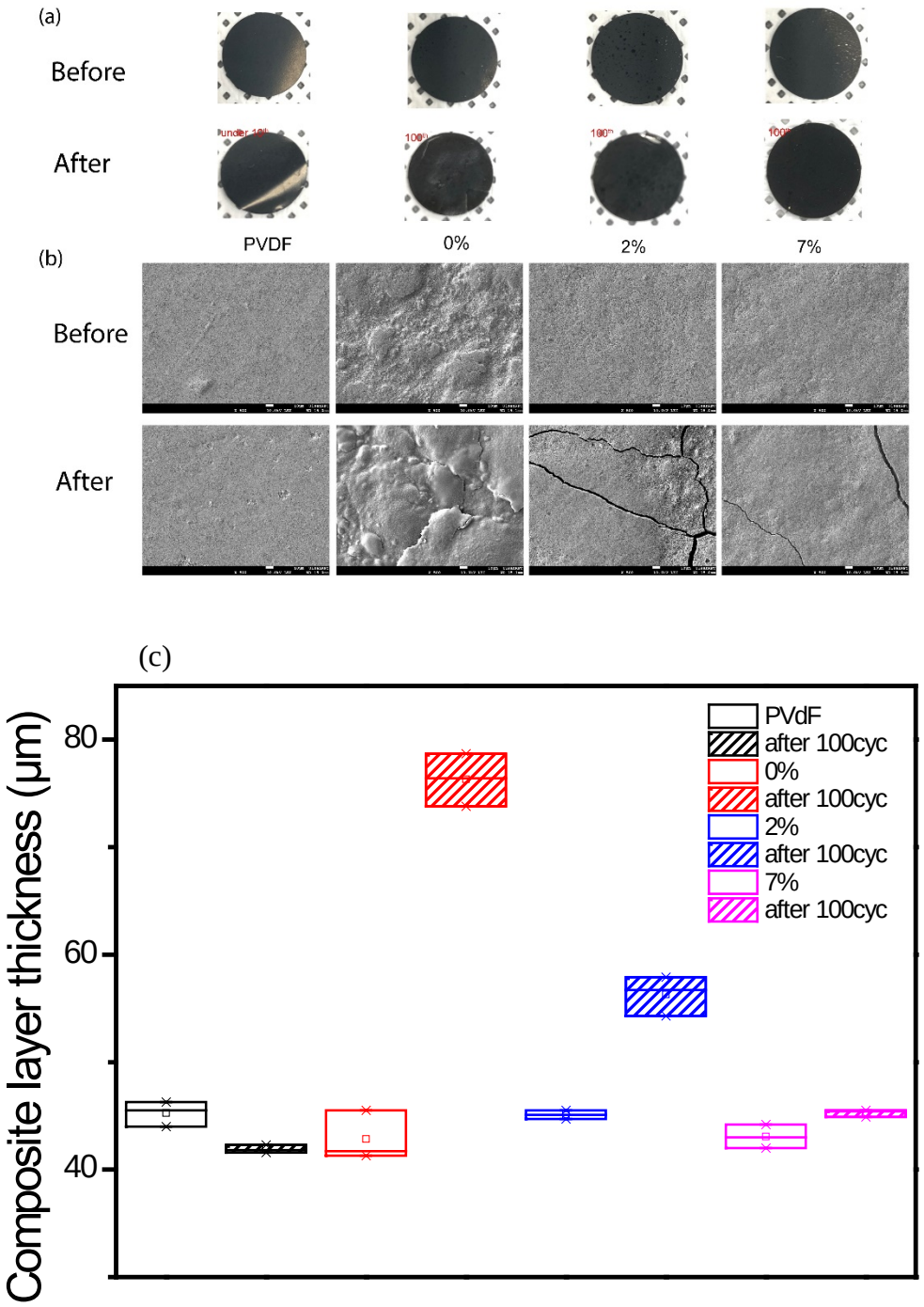

Figure 22. LFP electrode with different binders before and after 100 cycles: (a) photo-image of the electrode, (b) Top FE-SEM image with ×2000 magnifications and (c) difference of composite layer thickness

4. Conclusion

In this study Styrenesulfonic acid Sodium Salt hydrate (NaSS), a monomer for improving ionic conductivity, was applied to the cathode and anode, the battery performance was compared and analyzed through electrochemical evaluation.

As a result of analyzing the ionic conductivity by applying a functional group (SO_3H) containing a lone pair to the binder, the ionic conductivity increases. After synthesis confirmed by particle size, zeta potential and FT-IR. Compared to 0% sample, the percentage of NaSS is increased Li^+ ion transport numbers by twice and ionic conductivity by increased 10times. And surface of binder with NaSS is familiar to the electrolyte, low contact angle and increase wettability of the electrolyte.

PS/NaSS based binder is applied for both of commercial graphite anode and LFP cathode electrode, it is loading that the binder shows achievement electrochemical performance compared to without NaSS sample and commercial PVdF binder. Graphite anode with PS/NaSS is higher adhesion ability following lower interface resistance. That is loaded 320 mAh/g of specific capacity compared to that electrode with PS binder, 303 mAh/g after 100 cycles. LFP cathode with PS/NaSS is higher adhesion ability following lower interface resistance. That is loaded 135 mAh/g of specific capacity compared to that electrode with PS binder (101 mAh/g) and with PVdF (10 mAh/g) after 100cycles.

As the result, PS/NaSS binder can be applied to cathode and anode electrodes, high contained PS/NaSS binder such as 7% sample has been showing better electrochemical stability than 2% sample.

5. Reference

[1] N. Yabuuchi, M. Takeuchi, M. Nakayama, H. Shiiba, M. Ogawa, K. Nakayama, T. Ohta, D. Endo, T. Ozaki, T. Inamasu, K. Sato, S. Komaba, High-capacity electrode materials for rechargeable lithium batteries: Li3NbO4-based system with cation-disordered rocksalt structure, Proc. Natl. Acad. Sci. 112 (2015) 7650–7655. https://doi.org/10.1073/pnas.1504901112.

[2] D. Gupta, G.M. Koenig, Analysis of Chemical and Electrochemical Lithiation/Delithiation of a Lithium-Ion Cathode Material, J. Electrochem. Soc. 167 (2020) 020537. https://doi.org/10.1149/1945-7111/ab6bbf.

[3] J. Duan, X. Tang, H. Dai, Y. Yang, W. Wu, X. Wei, Y. Huang, Building Safe Lithium-Ion Batteries for Electric Vehicles: A Review, Electrochem. Energy Rev. 3 (2020) 1–42. https://doi.org/10.1007/s41918-019-00060-4.

[4] L. Chen, L.L. Shaw, Recent advances in lithium–sulfur batteries, J. Power Sources. 267 (2014) 770–783. https://doi.org/10.1016/j.jpowsour.2014.05.111.

[5] H. Kim, J. Hong, Y.-U. Park, J. Kim, I. Hwang, K. Kang, Sodium Storage Behavior in Natural Graphite using Ether-based Electrolyte Systems, Adv. Funct. Mater. 25 (2015) 534–541. https://doi.org/10.1002/adfm.201402984.

[6] Y. Sun, G. Zheng, Z.W. Seh, N. Liu, S. Wang, J. Sun, H.R. Lee, Y. Cui, Graphite-Encapsulated Li-Metal Hybrid Anodes for High-Capacity Li Batteries, Chem. 1 (2016) 287–297. https://doi.org/10.1016/j.chempr.2016.07.009.

[7] R. Schmuch, R. Wagner, G. Hörpel, T. Placke, M. Winter, Performance and cost of materials for lithium-based rechargeable automotive batteries, Nat. Energy. 3 (2018) 267–278. https://doi.org/10.1038/s41560-018-0107-2.

[8] T. Kim, W. Song, D.-Y. Son, L.K. Ono, Y. Qi, Lithium-ion batteries: outlook on present, future, and hybridized technologies, J. Mater. Chem. A. 7 (2019) 2942–2964. https://doi.org/10.1039/C8TA10513H.

[9] Y. Ding, Z.P. Cano, A. Yu, J. Lu, Z. Chen, Automotive Li-Ion Batteries: Current Status and Future Perspectives, Electrochem. Energy Rev. 2 (2019) 1–28. https://doi.org/10.1007/s41918-018-0022-z.

[10] P. Guan, L. Zhou, Z. Yu, Y. Sun, Y. Liu, F. Wu, Y. Jiang, D. Chu, Recent progress of surface coating on cathode materials for high-performance lithium-ion batteries, J. Energy Chem. 43 (2020) 220–235. https://doi.org/10.1016/j.jechem.2019.08.022.

[11] M. Li, J. Lu, Z. Chen, K. Amine, 30 Years of Lithium-Ion Batteries, Adv. Mater. 30 (2018) 1800561. https://doi.org/10.1002/adma.201800561.

[12] J. Fang, L. Fan, J. Zhang, M. Deng, G. Xie, The Blocking Properties of Styrene-Styrene Sulfonic Acid Sodium Salt Copolymer as a Nanodispersing Agent in Water-Based Drilling Fluids, Chem. Technol. Fuels Oils. 57 (2021) 95–106. https://doi.org/10.1007/s10553-021-01230-1.

[13] J. Shen, H. Wang, Y. Zhou, N. Ye, G. Li, L. Wang, Anatase/ rutile TiO 2 nanocomposite microspheres with hierarchically porous structures for high-performance lithium-ion batteries, RSC Adv. 2 (2012) 9173–9178. https://doi.org/10.1039/C2RA20962D.

[14] S. Yang, X. Zhou, J. Zhang, Z. Liu, Morphology-controlled solvothermal synthesis of LiFePO4 as a cathode material for lithium-ion batteries, J. Mater. Chem. 20 (2010) 8086–8091. https://doi.org/10.1039/C0JM01346C.

[15] J.-H. Jeong, D. Jung, E.W. Shin, E.-S. Oh, Boron-doped TiO2 anode materials for high-rate lithium ion batteries, J. Alloys Compd. 604 (2014) 226–232.

https://doi.org/10.1016/j.jallcom.2014.03.069.

[16] M. Sun, H. Zhong, S. Jiao, H. Shao, L. Zhang, Investigation on Carboxymethyl Chitosan as New Water Soluble Binder for LiFePO4 Cathode in Li-Ion Batteries, Electrochimica Acta. 127 (2014) 239–244. https://doi.org/10.1016/j.electacta.2014.02.027.

[17] N. Takami, A. Satoh, M. Hara, T. Ohsaki, Structural and Kinetic Characterization of Lithium Intercalation into Carbon Anodes for Secondary Lithium Batteries, J. Electrochem. Soc. 142 (1995) 371–379. https://doi.org/10.1149/1.2044017.

[18] C. Lin, X. Fan, Y. Xin, F. Cheng, M.O. Lai, H. Zhou, L. Lu, Li4Ti5O12-based anode materials with low working potentials, high rate capabilities and high cyclability for high-power lithium-ion batteries: a synergistic effect of doping, incorporating a conductive phase and reducing the particle size, J. Mater. Chem. A. 2 (2014) 9982–9993. https://doi.org/10.1039/C4TA01163E.

[19] M.K. Mohanapriya, K. Deshmukh, K. Chidambaram, M.B. Ahamed, K.K. Sadasivuni, D. Ponnamma, M.A.-A. AlMaadeed, R.R. Deshmukh, S.K.K. Pasha, Polyvinyl alcohol (PVA)/polystyrene sulfonic acid (PSSA)/carbon black nanocomposite for flexible energy storage device applications, J. Mater. Sci. Mater. Electron. 28 (2017) 6099–6111. https://doi.org/10.1007/s10854-016-6287-2.

[20] D.S. Kim, H.B. Park, J.W. Rhim, Y. Moo Lee, Preparation and characterization of crosslinked PVA/SiO2 hybrid membranes containing sulfonic acid groups for direct methanol fuel cell applications, J. Membr. Sci. 240 (2004) 37–48. https://doi.org/10.1016/j.memsci.2004.04.010.

[21] B.T.N.C. Andrade, A.C. da S. Bezerra, C.R. Calado, Adding value to polystyrene waste by chemically transforming it into sulfonated polystyrene, Matér. Rio Jan. 24 (2019).

https://doi.org/10.1590/S1517-707620190003.0732.

[22] S.B. Brijmohan, S. Swier, R.A. Weiss, M.T. Shaw, Synthesis and Characterization of Cross-linked Sulfonated Polystyrene Nanoparticles, Ind. Eng. Chem. Res. 44 (2005) 8039–8045. https://doi.org/10.1021/ie050703v.

[23] S. Chauque, F.Y. Oliva, O.R. Cámara, R.M. Torresi, Use of poly[ionic liquid] as a conductive binder in lithium ion batteries, J. Solid State Electrochem. 22 (2018) 3589–3596. https://doi.org/10.1007/s10008-018-4078-9.

[24] Y. Qi, M.H.T. Nguyen, E.-S. Oh, Effect of conductive polypyrrole in poly(acrylonitrile-co-butyl acrylate) water–based binder on the performance of electrochemical double-layer capacitors, J. Solid State Electrochem. (2020). https://doi.org/10.1007/s10008-020-04864-z.

[25] J. He, L. Zhang, Polyvinyl alcohol grafted poly (acrylic acid) as water-soluble binder with enhanced adhesion capability and electrochemical performances for Si anode, J. Alloys Compd. 763 (2018) 228–240. https://doi.org/10.1016/j.jallcom.2018.05.286.

[26] T. Zhao, L. Jiang, Contact angle measurement of natural materials, Colloids Surf. B Biointerfaces. 161 (2018) 324–330. https://doi.org/10.1016/j.colsurfb.2017.10.056.

[27] R.S. Hebbar, A.M. Isloor, A.F. Ismail, Chapter 12 - Contact Angle Measurements, in: N. Hilal, A.F. Ismail, T. Matsuura, D. Oatley-Radcliffe (Eds.), Membr. Charact., Elsevier, 2017: pp. 219–255. https://doi.org/10.1016/B978-0-444-63776-5.00012-7.